

UNIVERSIDADE FEDERAL DE MINAS GERAIS

Curso de Pós-Graduação em Engenharia Metalúrgica, Materiais e de Minas – Mestrado
Profissional

Dissertação de Mestrado

DEVELOPMENT AND APPLICABILITY OF A NOVEL TEST TO EVALUATE THE
CORROSION RESISTANCE OF MAGNESIA REFRACTORIES TO GASEOUS
SULFUR OXIDES

Autora: Daniela Mancini Fonseca

Orientador: Prof. Eduardo Henrique Martins Nunes

Dezembro de 2020

Daniela Mancini Fonseca

Daniela Mancini Fonseca

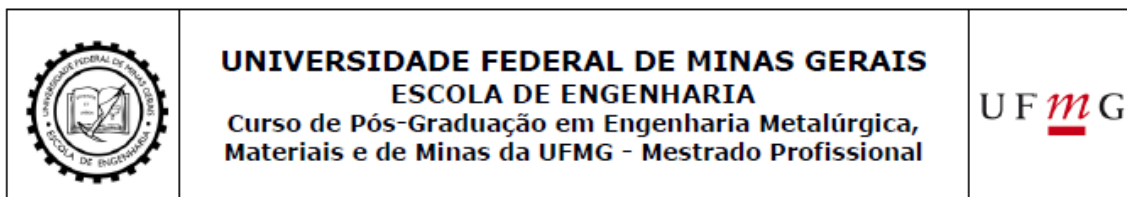
DEVELOPMENT AND APPLICABILITY OF A NOVEL TEST TO EVALUATE THE CORROSION
RESISTANCE OF MAGNESIA REFRACTORIES TO GASEOUS SULFUR OXIDES

Dissertação apresentada ao Curso de Pós-Graduação em Engenharia Metalúrgica, Materiais e de Minas – Mestrado Profissional da Escola de Engenharia da Universidade Federal de Minas Gerais, como requisito parcial para obtenção do Grau de Mestre em Engenharia Metalúrgica, Materiais e de Minas.

Área de concentração: Engenharia de Materiais/ Materiais Cerâmicos, Poliméricos, Compósitos e Recobrimentos
Orientador: Prof. Eduardo Henrique Martins Nunes

Belo Horizonte
Universidade Federal de Minas Gerais
Escola de Engenharia
2020

| | |
|-------|---|
| F676d | <p>Fonseca, Daniela Mancini. Development and applicability of a novel test to evaluate the corrosion resistance of magnesia refractories to gaseous sulfur oxides [recurso eletrônico] / Daniela Mancini Fonseca. - 2020. 1 recurso online (xiv, 71 f. : il., color.) : pdf.</p> <p>Orientador: Eduardo Henrique Martins Nunes.</p> <p>Dissertação (mestrado profissional) - Universidade Federal de Minas Gerais, Escola de Engenharia.</p> <p>Apêndices: f. 69-71.</p> <p>Bibliografia: f. 65-68. Exigências do sistema: Adobe Acrobat Reader.</p> <p>1. Materiais - Teses. 2. Ciência dos materiais - Teses. 3. Corrosão - Teses. 4. Materiais refratários - Teses. 5. Sulfato - Teses. I. Nunes, Eduardo Henrique Martins. II. Universidade Federal de Minas Gerais. Escola de Engenharia. III. Título.</p> <p style="text-align: right;">CDU: 620(043)</p> |
|-------|---|



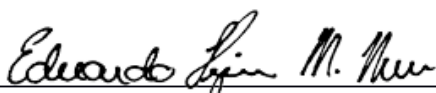
**DEVELOPMENT AND APPLICABILITY OF A NOVEL TEST TO
EVALUATE THE CORROSION RESISTANCE OF MAGNESIA
REFRACTORIES TO GASEOUS SULFUR OXIDES**

DANIELA MANCINI FONSECA

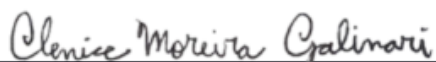
Dissertação submetida à Comissão Examinadora designada pelo Colegiado do Curso de Pós-Graduação em Engenharia Metalúrgica, Materiais e de Minas da UFMG – Mestrado Profissional da Universidade Federal de Minas Gerais como requisito parcial para obtenção do grau de Mestre em Engenharia Metalúrgica, Materiais e de Minas.

Aprovada em 18 de dezembro de 2020.

Por:



Prof. Eduardo Henrique Martins Nunes, Dr. (UFMG)
Orientador



Clenice Moreira Galinari, Dr.^a (RHI Magnesita)



Prof. Sergio Luiz Cabral da Silva, Dr. (UFMG)

AGRADECIMENTOS

A autora agradece a todos aqueles que, direta ou indiretamente, colaboraram na preparação deste trabalho. Em particular, ao professor Eduardo Henrique Martins Nunes, pela disponibilidade, apoio e ensinamentos, mesmo de longe. Sinto-me grata pela oportunidade de ter você como meu orientador e, através desse trabalho, ajudar a estreitar os laços entre a universidade e a indústria. Aos meus pais, por me ensinar a importância do constante aprendizado e desenvolvimento pessoal e profissional, além das valiosas contribuições ao presente trabalho. À minha irmã, Juliana, e ao Gabriel, pelo amor, companheirismo e amizade durante toda essa jornada. Aos colegas da RHI Magnesita, pela consultoria técnica durante o percurso e a disposição para desbravar comigo novos caminhos.

RESUMO

A degradação de revestimentos refratários por gases de enxofre é um dos principais mecanismos de desgaste dos revestimentos utilizados na indústria do cobre. Os gases SO_2/SO_3 infiltram-se nos poros dos tijolos refratários básicos, combinam-se com suas matérias primas através de reações expansivas, causam a densificação de sua face fria e podem levar à falha precoce dos mesmos. Neste trabalho é introduzido um procedimento novo, simples, econômico e confiável para avaliar a resistência química de refratários básicos a gases sulfurosos. Este teste é baseado na avaliação da densidade e porosidade aparente de amostras de tijolos básicos antes e após tratamento térmico em atmosfera rica em SO_2/SO_3 . Foi demonstrado que quanto maior a variação destas propriedades, menor a resistência à corrosão do refratário. Este método foi também empregado para investigar a influência da relação CaO/SiO_2 (C/S) na resistência química e propriedades físicas dos tijolos refratários. Amostras com relação C/S abaixo de 0,5 mostraram maior resistência à corrosão devido à presença de forsterita (Mg_2SiO_4) como a fase intersticial primária, a qual não reage com os gases de enxofre para formar sulfatos de magnésio e cálcio. A geração de tais sulfatos pode causar o bloqueio parcial da estrutura dos poros e levar à sua falha por termoclase estrutural. Foi demonstrado que a porosidade aparente inicial do refratário também desempenha um papel importante na resistência à corrosão da amostra. Este novo procedimento forneceu resultados consistentes e estatisticamente significativos que estão de acordo tanto com o comportamento comumente observado durante a operação quanto com os resultados relatados em estudos post-mortem anteriores. Esta ferramenta pode ser muito útil para selecionar refratários para a indústria de não-ferrosos e prever seu desempenho.

PALAVRAS-CHAVE: sulfato; corrosão; ataque por enxofre; refratários básicos; relação CaO/SiO_2

ABSTRACT

The degradation of refractory linings by sulfur gases is one of the main lining wear mechanisms observed in the copper industry. SO_2/SO_3 gases infiltrate into the pore structure of basic refractory bricks, combine with their raw materials through expansive reactions leading to the densification of their cold face, and possibly cause premature failure of the refractory lining. A novel, simple, cost-effective, and reliable procedure to evaluate the chemical resistance of basic refractories to sulfur gases is introduced in this work. This test is based on the measurement of apparent porosity and bulk density of MgO-based samples before and after heat treatment in an SO_2/SO_3 -rich atmosphere. It was demonstrated that the more considerable the variation in these properties, the lower the corrosion resistance of the refractory. This method was used to investigate the influence of the CaO to SiO_2 (C/S) ratio on the chemical resistance and physical properties of refractory bricks. Samples with C/S ratios below 0.5 showed higher corrosion resistance due to the presence of forsterite (Mg_2SiO_4) as the primary interstitial phase, which does not react with the sulfur gases to form magnesium and calcium sulfates. The generation of such sulfates may cause partial blocking of the pore structure and lead to spalling of the refractory lining. It was shown that the refractory's initial apparent porosity also plays a significant role in the sample's corrosion resistance. This novel procedure provided consistent and statistically significant results, which are in line with the behavior commonly observed during operation and the findings reported in previous post-mortem studies. This test could be beneficial to select refractory grades for the non-ferrous industry and predict their performance.

KEYWORDS: sulfate; corrosion; sulfur attack; basic refractories; CaO/ SiO_2 ratio

LIST OF FIGURES

| | |
|--|----|
| Figure 1.1: Example of a copper flash smelting furnace refractory project | 15 |
| Figure 1.2: Brick taken from a nickel flash smelting furnace, showing cracks parallel to its hot face | 16 |
| Figure 1.3: SEM analysis of the hot face of a refractory brick from a nickel flash smelting furnace (section 1 in Figure 1.1). | 17 |
| Figure 1.4: Optical microscopy and SEM analysis of the brick from a copper concentrate smelting furnace | 17 |
| Figure 1.5: Brick taken from an Isasmelt furnace, showing matte infiltration and spalling in the hot face. | 18 |
| Figure 1.6: SEM micrographs of (a) the hot face and (b) cold face of the brick displayed in Figure 1.5. | 18 |
| Figure 3.1: Schematic diagram of the different processes and approaches used to produce primary copper..... | 25 |
| Figure 3.2: Schematic diagram of the primary copper production process. | 26 |
| Figure 3.3: Illustration of the steps involved in primary copper production..... | 26 |
| Figure 3.4: CaO-MgO-SiO ₂ phase diagram calculated in FactSage™..... | 31 |
| Figure 3.5: Parameters used for evaluating the bulk density and apparent porosity of refractory bricks. | 35 |
| Figure 3.6: Schematic representation of the corrosion of basic refractories by sulfur gases during copper smelting..... | 37 |
| Figure 4.1: Schematic diagram of the test procedure | 42 |
| Figure 4.2: Setup used in the corrosion tests..... | 43 |
| Figure 4.3: Closed box containing the sample bricks and positioned inside a furnace..... | 43 |
| Figure 4.4: Test temperature and final decomposition temperatures estimated for Al ₂ (SO ₄) ₃ , MgSO ₄ , and CaSO ₄ (dashed lines)..... | 44 |
| Figure 5.1: Simulation performed on the FactSage™ software to evaluate the volume of the liquid phase formed in different samples at temperatures ranging from 1450 to 1630 °C..... | 47 |

- Figure 5.2:** AP and CCS as a function of the C/S ratio and sintering temperature. Inset: pore size distribution of sample C0 sintered in air at 1450, 1550, and 1630 °C. 48
- Figure 5.3:** Visual aspect of the refractory samples after corrosion test I..... 49
- Figure 5.4:** Variation in AP and BD as a function of the C/S ratio evaluated considering the values obtained before and after the corrosion tests. The SO₃ concentration in the tested materials is also shown. 51
- Figure 5.5:** XRD patterns of samples C0 to C6 after the corrosion test 54
- Figure 5.6:** XRD patterns of C0 and C6 before (as-prepared) and after the corrosion test..... 55
- Figure 5.7:** OM micrographs of C0 and C6 before (as-prepared) and after the corrosion tests 56
- Figure 5.8:** Backscattered electron SEM micrograph of C0 before (as-prepared) and after the corrosion test..... 57
- Figure 5.9:** Variation in AP, BD, and SO₃ content as a function of the firing temperature and initial apparent porosity for sample C5..... 58

LIST OF TABLES

| | |
|--|----|
| Table III.1: Relative thermal stability of some sulfates based on the equilibrium partial pressure of SO ₃ at 727 °C..... | 23 |
| Table III.2: Initial decomposition temperatures (°C) of metal sulfates under air or nitrogen flow at heating rates of 2 or 5° C.min ⁻¹ | 23 |
| Table III.3: Decomposition temperature range for some metal sulfates according to various studies assessed by Kellogg | 24 |
| Table III.4: Expected main phases formed for different molar CaO/ SiO ₂ ratios in systems containing high MgO content..... | 31 |
| Table III.5: Overall comparison of the main properties of the different classes of magnesia-chromite bricks. | 32 |
| Table IV.1: Refractory compositions used in this study and their calculated C/S ratios | 39 |
| Table IV.2: Corrosion tests conducted in this study and their objectives. | 40 |
| Table V.1: Chemical composition obtained by XRF for the materials fabricated in this study. Examinations conducted on as-prepared samples..... | 46 |
| Table V.2: F ratios and p-values obtained by one-way ANOVA for the comparison of samples C0 to C6 regarding the following properties: change in bulk density, change in apparent porosity, and sulfur content. | 51 |
| Table V.3: p-values obtained by Fisher's Protected LSD test for the comparison of samples C0 to C6 regarding the following properties: change in bulk density, change in apparent porosity, and sulfur content. | 52 |
| Table V.4: F ratios and p-values obtained by repeated measures ANOVA for the comparison of samples C5 fired at 1450 °C, 1550 °C, and 1630 °C regarding the change in bulk density and change in apparent porosity. | 58 |
| Table V.5: Variation in AP, BD and SO ₃ content as a function of the firing temperature and initial apparent porosity for samples C0 and C6 | 59 |
| Table XX.1: Bulk density, apparent porosity and cold crushing strength results of the original samples C0-C6 and RS after each firing temperature | 69 |
| Table XX.2: Weight of the samples before and after the last two tests of corrosion test I | 69 |
| Table XX.3: Bulk density and apparent porosity of the original samples and the percentual change after each test (including SO ₃ content) of corrosion test I..... | 70 |

| | |
|--|----|
| Table XX.4: Changes in bulk density and apparent porosity and SO ₃ / MgSO ₄ content of composition C5 after the corrosion test II | 71 |
|--|----|

LIST OF ACRONYMS

- AP: apparent porosity.

- BD: bulk density.

- CCS: cold crushing strength.

- C/S ratio: molar ratio of CaO to SiO₂.

- XRD: X-ray diffraction.

- XRF: X-ray fluorescence.

TABLE OF CONTENTS

| | |
|--|----|
| 1. INTRODUCTION | 15 |
| 2. OBJECTIVES | 21 |
| 3. BACKGROUND..... | 22 |
| 3.1 SULFATES | 22 |
| 3.2 PRIMARY COPPER PRODUCTION | 25 |
| 3.2.1 SMELTING..... | 26 |
| 3.2.2 CONVERTING | 27 |
| 3.2.3 REFINING | 28 |
| 3.2.4 ELECTROREFINING..... | 29 |
| 3.3 FIRED MAGNESIA-BASED REFRACTORY BRICKS | 30 |
| 3.3.1 MAGNESIA BRICKS..... | 30 |
| 3.3.2 MAGNESIA-CHROMITE BRICKS..... | 32 |
| 3.3.3 MAGNESIA-SPINEL BRICKS | 33 |
| 3.3.4 DOLOMA BRICKS | 33 |
| 3.4 REFRACTORY TESTING | 34 |
| 3.4.1 BULK DENSITY AND APPARENT POROSITY | 34 |
| 3.4.2 COLD CRUSHING STRENGTH | 35 |
| 3.4.3 X-RAY FLUORESCENCE SPECTROMETRY AND SULFUR ELEMENTAL ANALYSIS | 35 |
| 3.4.4 X-RAY DIFFRACTION | 36 |
| 3.4.5 CORROSION OF BASIC REFRACTORIES BY SULFUR GASES | 36 |
| 4. MATERIALS AND METHODS..... | 39 |
| 4.1 SAMPLE PREPARATION AND SELECTION..... | 39 |
| 4.2 CORROSION RESISTANCE..... | 41 |
| 4.2.1 TESTING PROCEDURE | 41 |
| 4.2.2 QUANTITATIVE ANALYSIS..... | 44 |
| 4.2.3 QUALITATIVE ANALYSIS..... | 45 |
| 5. RESULTS AND DISCUSSION | 46 |

| | |
|--|----|
| 5.3 CORROSION TEST I..... | 49 |
| 5.4 CORROSION TEST II..... | 57 |
| 5.5 CORROSION TEST III..... | 59 |
| 6. CONCLUSIONS | 61 |
| 7. SUGGESTIONS FOR FUTURE WORKS | 63 |
| 8. ACADEMIC PRODUCTION RELATED TO THIS WORK..... | 64 |
| 9. REFERENCES..... | 65 |
| 10. APPENDIX..... | 69 |

1. INTRODUCTION

The oxidation of sulfides during the production of non-ferrous metals leads to the formation of sulfur oxides, which infiltrate into the refractory lining pore structure and react with basic oxides at temperatures below 1000 °C, giving rise to magnesium and calcium sulfates. This reaction is accompanied by an expressive volume increase, densification of the refractory microstructure, and weakening of the brick bond ⁽¹⁾. It is well established that the corrosion of refractories by SO₂/SO₃ is an important wear mechanism in the non-ferrous industry, and the corrosion resistance of refractories to gaseous sulfur oxides should be considered when defining the optimal lining for this application. Several post-mortem studies of magnesia-chromite refractories used in the non-ferrous industry were performed over the past 35 years at RHI Magnesita. In about 25% of these studies, the corrosion caused by sulfur oxides was detected as a relevant cause of lining failure, along with fayalitic slag infiltration and spalling, which are the most common wear mechanisms. Examples of such post-mortem studies are provided in this work to demonstrate the importance of this wear mechanism. Figure 1.1 shows an example of refractory lining used in the non-ferrous industry. The brick's hot face (surface facing the inside of the equipment) and cold face (opposite surface) are indicated, together with the intake shaft through which the sulfur gases are conducted.

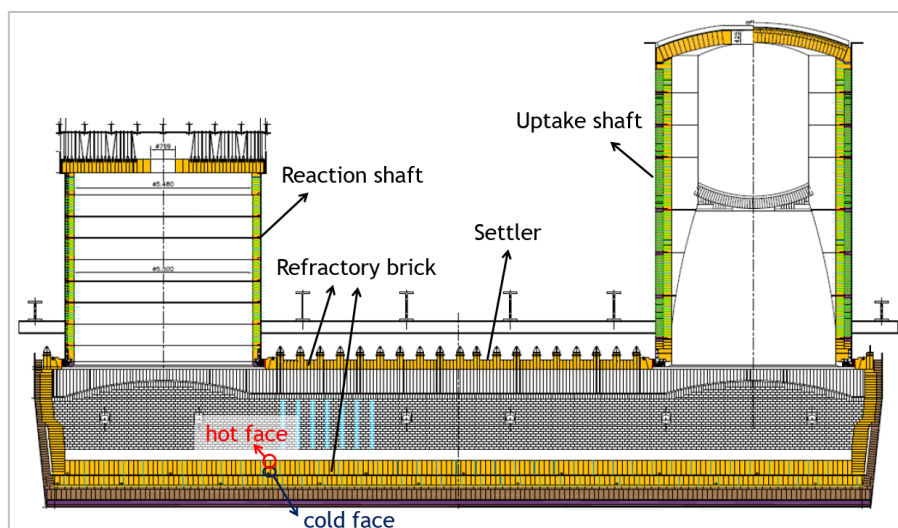


Figure 1.1: Example of a copper flash smelting furnace refractory project

A direct-bonded magnesia-chromite brick used in the reaction shaft roof of a nickel flash smelting furnace was investigated in 2004 ⁽²⁾ due to the roof lining's premature wear. Several cracks were observed parallel to the brick's hot face, as indicated by the arrows displayed in Figure 1.2. The chemical analysis of this sample revealed about 6 wt.% of SO_3 in its hot face. The microstructural investigation revealed corrosion of magnesia and the calcium-rich secondary phases due to the action of sulfur gases (Figure 1.3). The main wear mechanism of the magnesia-chromite brick investigated in this study was structural spalling and corrosion caused mainly by the sulfur attack. The corrosion of the brick by SO_2 resulted in cracking due to both high densification of its microstructure and weakening of the brick's bonds.



Figure 1.2: Brick taken from a nickel flash smelting furnace, showing cracks parallel to its hot face (arrows). Sections were cut from the hot face for microscopic ⁽¹⁾ and chemical (CA) examinations.

A co-clinker-based magnesia-chromite brick from the roof of a copper concentrate smelting furnace was investigated in 2015 ⁽³⁾. The brick's immediate hot face was missing due to spalling, and SO_3 was detected by sulfur elemental analysis in the sample at a concentration of 4.6 wt.% in the hot face and 1.1 wt.% in the cold face. The chemical and microscopical studies indicated the corrosion of interstitial phases due to a high sulfur supply ascribed to the presence of Na-Mg-K-sulfate and CaSO_4 (Figure 1.4). Pure magnesium sulfate was not detected, probably because the temperature

during the operation was at some point high enough to promote the decomposition of MgSO_4 . Such highly infiltrated and corroded bricks are susceptible to crack formation and spalling due to a discontinuous operation of the smelting furnace.

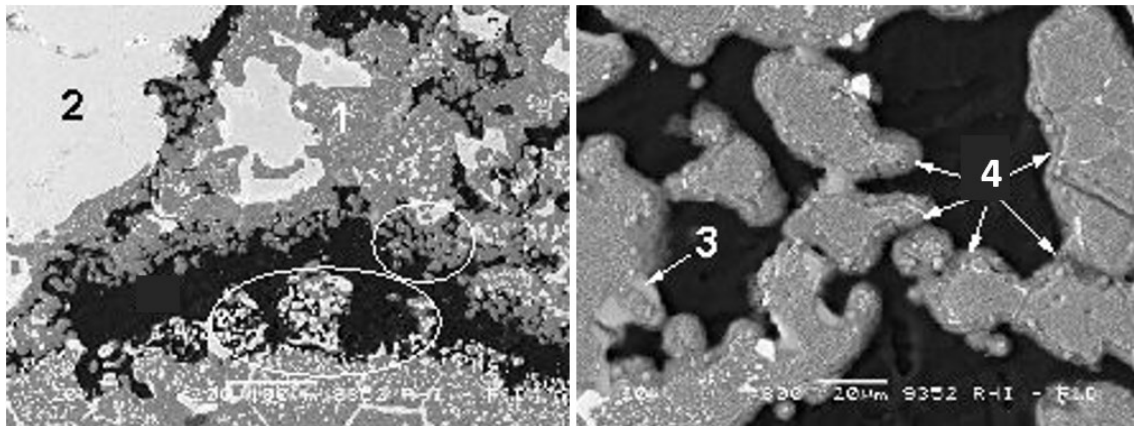


Figure 1.3: SEM micrographs (left: 220x; right: 800x) of the hot face of a refractory brick taken from a nickel flash smelting furnace (section 1 in Figure 1.1). Strongly corroded magnesia (circles); magnesia (1); chromite (2); Ca-sulfate (3); Mg-sulfate (4).

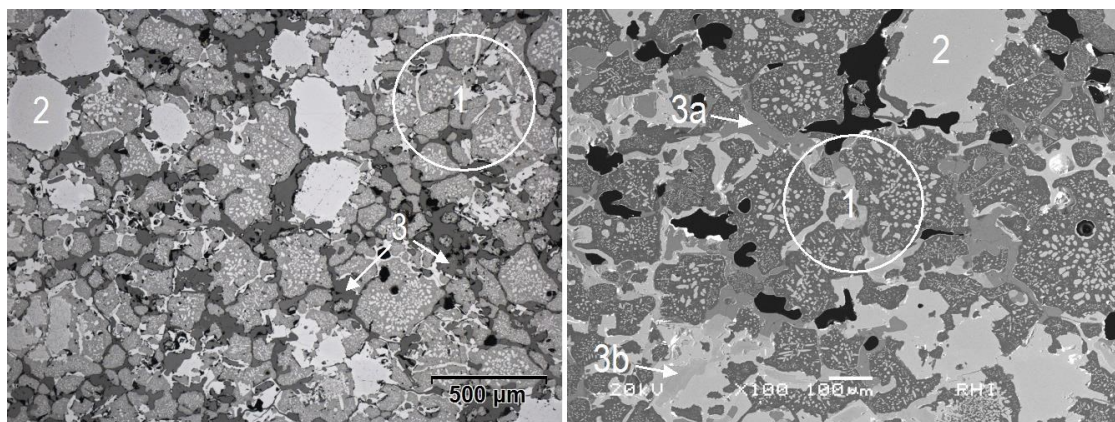


Figure 1.4: Optical microscopy (left: 50X) and SEM (right: 100X) analysis of the brick from a copper concentrate smelting furnace. Co-clinker (1); chromite (2); sulfate (3); Na-Mg-K-sulfate (3a); Ca-sulfate (3b).

Temperature fluctuations during the furnace operation can lead to magnesium sulfate decomposition, which gives rise to a porous MgO structure. Figure 1.5 shows an example of a direct bonded magnesia-chromite brick type MCr 50 (ISO 10081-2) taken from the upper shaft of a copper Isasmelt furnace ⁽⁴⁾. A severe change in the brick's

microstructure is observed. Calcium sulfate was formed at the interstice, and many magnesia grains were rimmed with the remnants of the magnesium sulfate decomposition (Figure 1.6).

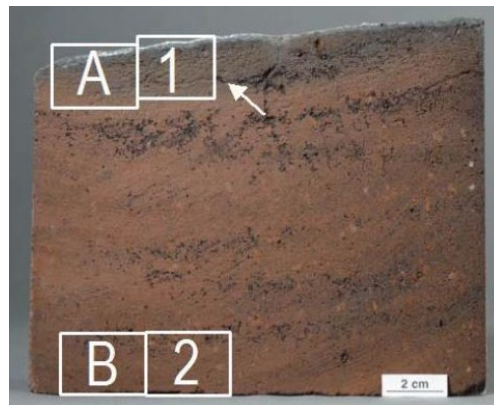


Figure 1.5: Brick taken from an Isasmelt furnace, showing matte infiltration and spalling in the hot face. A1 and B2 are the hot and cold faces, respectively.

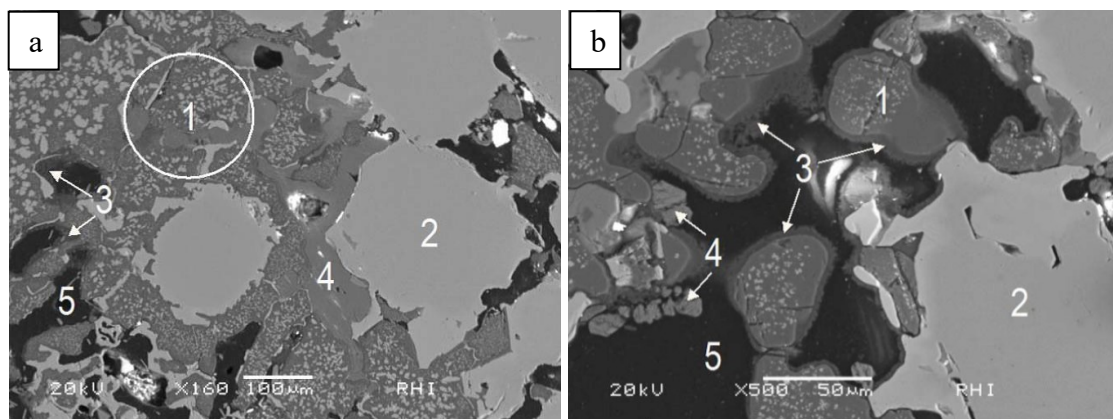


Figure 1.6: SEM micrographs (left: 160X; right: 500X) of (a) the hot face (A1) and (b) cold face (B2) of the brick displayed in Figure 1.5. (1) corroded magnesia; (2) chromite; (3) magnesia rings formed from the decomposition of magnesium sulfate; (4) calcium sulfate; (5) pore.

Alumina-chromia bricks are frequently recommended in areas where the bricks have little contact with slag and experience intense sulfur corrosion, such as in the roof of non-ferrous smelting furnaces. Since the operating temperature is usually above the decomposition temperature of aluminum sulfates, alumina-chromia bricks are much more resistant to the sulfur gases in the furnace's atmosphere than magnesia-based

bricks. However, they are more expensive (10-50%, depending on the brand) and less resistant to slag corrosion. Another alternative is to use magnesia-chromite bricks with low lime to silica (C/S) ratio. C/S ratios between 0 and 0.5 favor the formation of forsterite ($\text{MgO}\cdot\text{SiO}_2$) as the main interstitial phase, which generally leads to improved refractory performance in regions where there is a high sulfur gas supply. The literature review performed in the present work has shown that this phenomenon has not yet been proved or studied in detail.

Previous studies have focused on investigating the corrosion resistance of MgO-containing materials by sulfur oxides^(5; 6; 7; 8). The corrosion resistance to sulfur oxides of six commercially available basic refractories was evaluated in a semi-flow chemical reactor at 600, 800, and 1200 °C by measuring the relative increment of the specimens' mass over time⁽⁵⁾. The setup used in this study was complex and involved pressurized gas cylinders, a buffer tank, and many control and heating instruments. A magnesia-zirconia-forsterite material was considered the most resistant to sulfur oxides among the tested refractories⁽⁵⁾. A different study evaluated magnesite-chrome, chrome-magnesite, and magnesite refractories exposed to an $\text{SO}_2\text{-O}_2$ gas mixture at temperatures ranging from 700 to 1350 °C⁽⁶⁾. The experiments were conducted in a vertical tubular furnace under a controlled atmosphere for periods varying from 14 h to two weeks. The corrosion extent was evaluated based on gravimetric, chemical, and mineralogical analyses. The fused-grain magnesite-chrome refractory showed limited chemical attack by SO_2 -containing gases⁽⁶⁾. A previous dissertation of the same author developed at the University of the Witwatersrand⁽⁷⁾ investigated the reaction mechanisms of unused chrome-magnesite, magnesite-chrome, and magnesite refractories exposed to sulfur-bearing gas mixtures of $\text{SO}_2\text{-O}_2$, $\text{SO}_2\text{-N}_2$, and SO_2 at temperatures between 700 and 1350 °C. It was observed that the pore size, phase, and grain size distributions play an important role in the refractories' reactivity⁽⁷⁾. Another study attempted to describe the behavior of magnesia-spinel refractories in environments containing a high concentration of sulfur oxides at 500, 800, and 1000 °C⁽⁸⁾. Powdered samples consisting of different spinels were placed in a tubular furnace with flowing SO_2 -air mixture gas for up to 8 h. The mass increment of each sample was considered as a measure of the reaction progress. The findings

suggested that MgFe_2O_4 has a high reactivity compared to other spinels and MgO at $800\text{ }^\circ\text{C}$ ⁽⁸⁾.

The tests described in the literature so far involve expensive and complex methods that limit the applicability of such an evaluation procedure in the industrial context. The novel test suggested in this study was based on a previous method developed to assess alkali infiltration⁽⁹⁾ and provides a quantitative and straightforward procedure to evaluate the corrosion resistance of refractories to SO_2/SO_3 . Preliminary results were reported at two refractory conferences in 2018 and 2019⁽⁴⁾⁽¹⁰⁾. In this preliminary study, a box containing aluminum sulfate was used to evaluate the corrosion resistance to sulfur gases of seven different refractory samples at $900\text{ }^\circ\text{C}$. Recipes containing sintered MgO grains showed low corrosion resistance, followed by basic grades containing fused grains. Alumina-chromia grades were used as the reference and showed the highest resistance to this corrosion mechanism. Compared to the previously mentioned ones, limitations of this study include fixed temperature (evaluation of the corrosion resistance at lower temperatures is not possible) and fixed atmosphere (ratio of SO_3 cannot be determined nor varied). This work aims to consolidate this test method and determine the relationship between the lime to silica (C/S) ratio in magnesia refractories and their resistance to corrosion by sulfur oxides. This novel test is quite useful for comparing the corrosion resistance of different refractory recipes and adequately selecting the grades that should be employed in applications where sulfur gas corrosion plays a significant role.

2. OBJECTIVES

The main goals of this study are:

- Develop a new test to evaluate the corrosion resistance of refractory bricks to gaseous sulfur oxides.
- Compare refractory bricks with different CaO/SiO₂ ratios regarding their corrosion resistance.
- Determine the influence of the CaO/SiO₂ ratio and initial apparent porosity on the corrosion resistance of refractory bricks to sulfur gases.

3. BACKGROUND

Aiming to understand the objective of this work, a literature review covering five major topics is provided herein: (i) sulfates, (ii) primary copper production, (iii) fired magnesia-based refractory bricks, (iv) refractory testing, and (v) corrosion of basic refractories by sulfur gases. The literature review developed in this work focused on the primary copper production instead of other non-ferrous metals because it is the most consumed metal produced from sulfur-containing ores. Besides, copper is RHI Magnesita's most significant market within the non-ferrous industry.

3.1 SULFATES

Metal sulfates are salts consisting of a metal cation (M) such as Mg^{2+} , Al^{3+} and Ca^{2+} , and an SO_4^{2-} anion. The anion has a tetrahedral structure, which is distorted by the cation according to its polarizing power. Sulfates with small and highly electronegative cations are generally less stable than those containing large and poorly charged ions⁽¹¹⁾. All metal sulfates decompose to form SO_3 , which dissociates spontaneously to SO_2 and oxygen according to Eq. (2.1) and (2.2)⁽¹¹⁾:



Several studies have used experimental data to estimate the decomposition temperature of metal sulfates^(11; 12; 13; 8). Stern and Weise⁽¹¹⁾ measured the stability of several sulfates by calculating the partial and total pressures of the decomposition products (SO_3 , SO_2 , and O_2). Table III.1 shows the stability of some sulfates considered in this research according to the equilibrium partial pressure of SO_3 at 727 °C. According to this Table, $Al_2(SO_4)_3$ is the less stable sulfate. Its estimated decomposition temperature is between 727 and 827 °C, whereas $MgSO_4$ decomposes at temperatures around 1010 °C⁽¹¹⁾. Tagawa⁽¹²⁾ studied the thermal decomposition of sixteen different metal sulfates under air or nitrogen flow at heating rates of 2 and 5 °C.min⁻¹. The

results regarding the initial decomposition temperature of these sulfates are given in Table III.2.

Table III.1: Relative thermal stability of some sulfates based on the equilibrium partial pressure of SO₃ at 727 °C⁽¹¹⁾. The species are arranged in increasing order of stability.

| Sulfate | Product | P _{SO₃} (atm) |
|---|--------------------------------|-----------------------------------|
| Al ₂ (SO ₄) ₃ | Al ₂ O ₃ | 3.7 x 10 ⁻¹ |
| CuSO ₄ | CuO | 1.4 x 10 ⁻² |
| BeSO ₄ | BeO | 1.2 x 10 ⁻² |
| ZnSO ₄ | ZnO | 2.2 x 10 ⁻³ |
| Th(SO ₄) ₂ | ThO ₂ | 1.6 x 10 ⁻³ |
| MnSO ₄ | Mn ₃ O ₄ | 7.2 x 10 ⁻⁴ |
| PbSO ₄ | PbO (yellow) | 1.3 x 10 ⁻⁷ |
| CaSO ₄ | CaO | 4.7 x 10 ⁻¹² |
| BaSO ₄ | BaO | 1.5 x 10 ⁻¹⁷ |
| Na ₂ SO ₄ | Na ₂ O | 2.2 x 10 ⁻²² |

Table III.2: Initial decomposition temperatures (°C) of metal sulfates under air or nitrogen flow at heating rates of 2 or 5° C.min⁻¹⁽¹²⁾.

| Sulfate | Nitrogen | | Air | |
|---|------------------------|------------------------|------------------------|------------------------|
| | 2 °C.min ⁻¹ | 5 °C.min ⁻¹ | 2 °C.min ⁻¹ | 5 °C.min ⁻¹ |
| Al ₂ (SO ₄) ₃ | 493 | 500 | 516 | 524 |
| BeSO ₄ | 578 | 586 | 583 | 592 |
| CdSO ₄ | 759 | 778 | 783 | 783 |
| Ce(SO ₄) ₃ | 630 | 650 | 632 | 666 |
| Ce(SO ₄) ₂ | 340 | 379 | 377 | 383 |
| CoSO ₄ | 644 | 658 | 690 | 690 |
| CuSO ₄ | 538 | 561 | 586 | 605 |
| Fe ₂ (SO ₄) ₃ | 464 | 485 | 507 | 545 |
| La ₂ (SO ₄) ₃ | 772 | 782 | 790 | 817 |
| MgSO ₄ | 800 | 803 | 843 | 849 |
| MnSO ₄ | 650 | 693 | 687 | 717 |
| NiSO ₄ | 640 | 660 | 642 | 676 |
| ZnSO ₄ | 615 | 620 | 620 | 630 |
| Zn(SO ₄) ₂ | 382 | 435 | 386 | 438 |

Kellogg⁽¹³⁾ reviewed various experimental data regarding the reaction equilibrium as a function of temperature for different sulfates. The decomposition temperature range

for some metal sulfates according to this review is shown in Table III.3. A wide variation in the thermal decomposition behavior of many sulfates was detected. The most reliable experimental studies narrow down the decomposition temperature range for certain compounds as follows: from 572 to 777 °C for $\text{Al}_2(\text{SO}_4)_3$, from 1180 to 1370 °C for CaSO_4 , and from 950 to 1155 °C for MgSO_4 ⁽¹³⁾.

Table III.3: Decomposition temperature range for some metal sulfates according to various studies assessed by Kellogg⁽¹³⁾.

| Sulfate | Range (°C) |
|------------------------------|------------|
| $\text{Al}_2(\text{SO}_4)_3$ | 427-827 |
| CaSO_4 | 827-1370 |
| CuSO_4 | 427-827 |
| $\text{Fe}_2(\text{SO}_4)_3$ | 427-727 |
| MgSO_4 | 727-1155 |
| MnSO_4 | 427-827 |
| BeSO_4 | 627-827 |
| Na_2SO_4 | 327-884 |

Podwórny *et al.*⁽⁸⁾ performed kinetic experiments in a reactor to determine the dissociation pressure of different sulfates at different temperatures. Under the experiment conditions, the stability of each sulfate was determined as follows:

- MgSO_4 : $T < 1027$ °C
- $\text{Al}_2(\text{SO}_4)_3$: $T < 627$ °C
- $\text{Cr}_2(\text{SO}_4)_3$: $T < 727$ °C
- $\text{Fe}_2(\text{SO}_4)_3$: $T < 627$ °C

The most important factors influencing the decomposition process of metal sulfates are temperature, SO_3 partial pressure, metal oxide affinity to form sulfates, and retention time in the reaction vessel⁽¹⁴⁾. The exact decomposition temperature of common metal sulfates cannot be found in the literature because it depends on the conditions in which each experiment was performed.

3.2 PRIMARY COPPER PRODUCTION

Most of the copper produced worldwide derive from sulfide-based concentrates (primary production), mainly chalcopyrite (CuFeS_2), chalcocite (Cu_2S), and bornite (Cu_5FeS_4)⁽¹⁵⁾. About 80 % of this copper is produced from low-grade sulfide ores, which are usually treated by complex pyrometallurgical processes⁽¹⁾. Several different approaches are currently used to produce copper through different processes, as summarized in Figure 3.1⁽¹⁾.

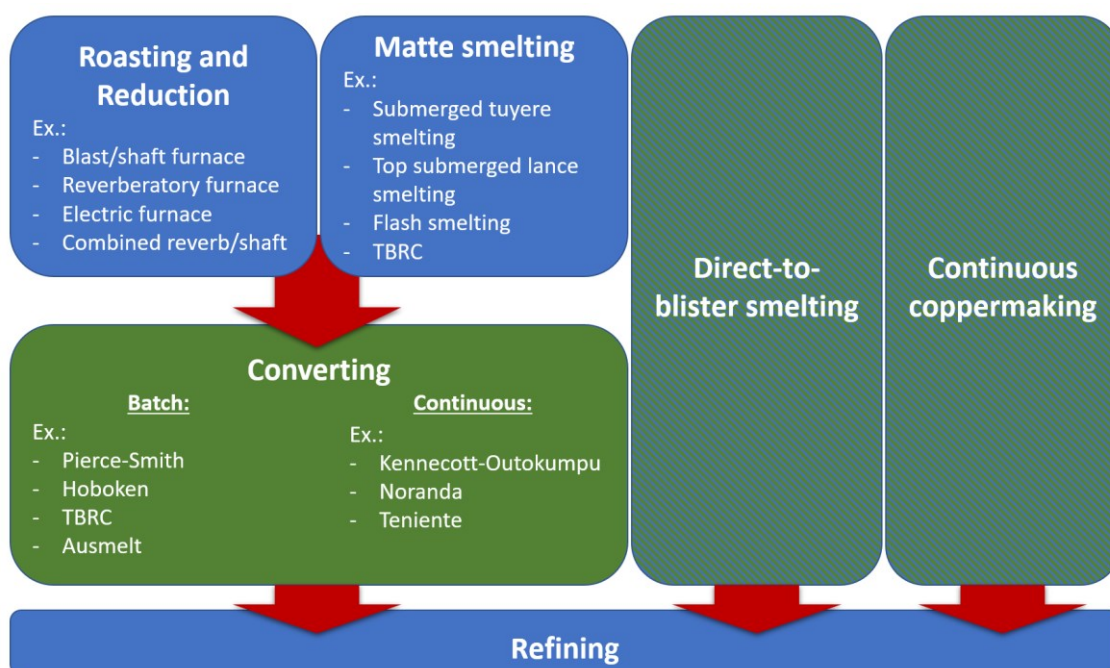


Figure 3.1: Schematic diagram of the different processes and approaches used to produce primary copper⁽¹⁾.

For simplicity, the process described in this section will involve flash smelting, batch converting (Hoboken), and refining. Figures 3.2 and 3.3 show a summary of the production process with the primary inputs and outputs in each step.

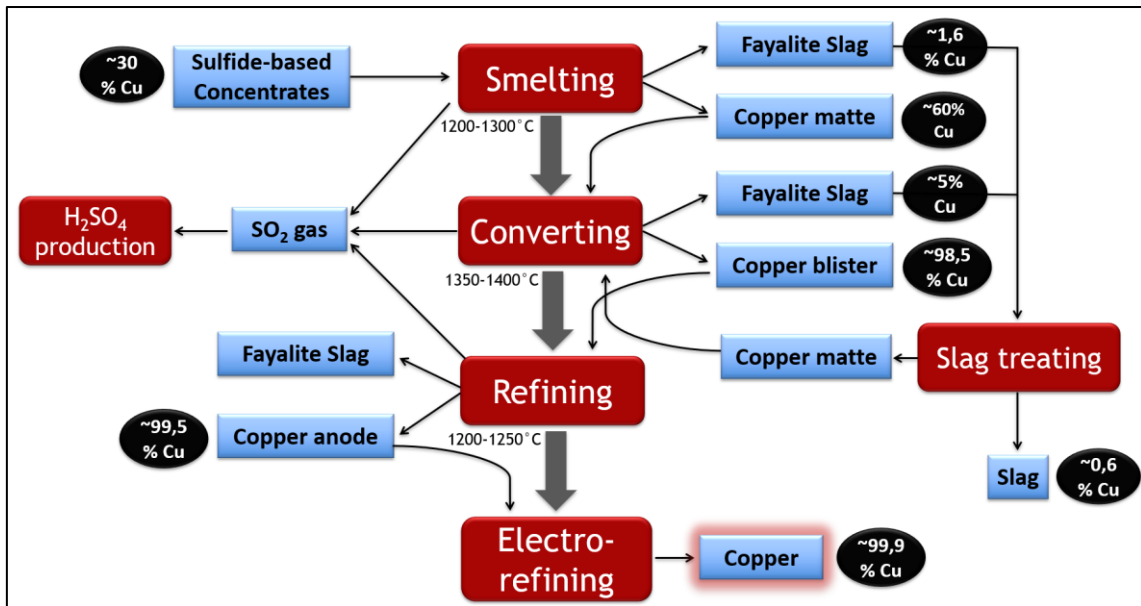


Figure 3.2: Schematic diagram of the primary copper production process.

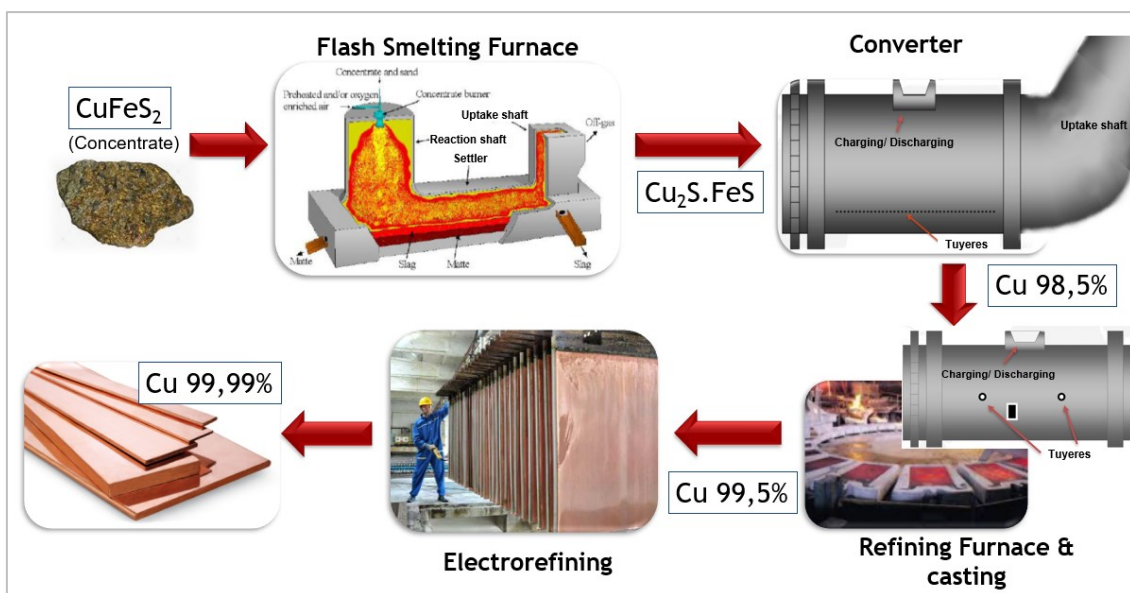
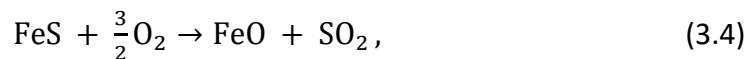
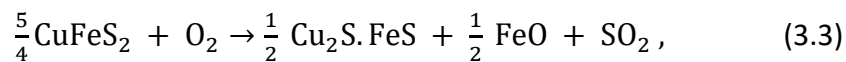


Figure 3.3: Illustration of the steps involved in primary copper production.

3.2.1 SMELTING

The flash furnace is considered one of the most efficient apparatus for this step ⁽¹⁾. Oxygen-enriched air gets in contact with the concentrate in the reaction shaft, and the outcome of this reaction is the copper matte ($\text{Cu}_2\text{S.FeS}$). Iron and sulfur present in the concentrate will react with oxygen and the silica sand added to the process, forming

fayalite (FeO.SiO₂) slag and SO₂. The gases produced in these reactions are released through the uptake shaft. Eq. (3.3) to (3.5) may take place during this step:

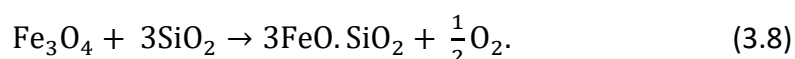
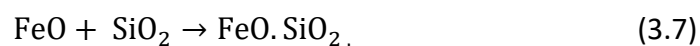
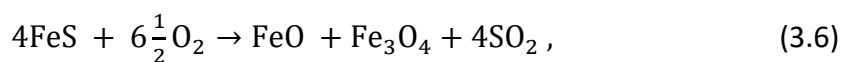


Magnesia-chromite bricks are often used as the working lining, and their campaign varies between 1.5 (reaction shaft), 5 (uptake shaft), and 3 years (settler)⁽¹⁶⁾.

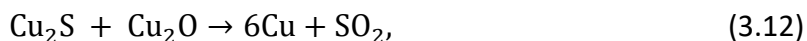
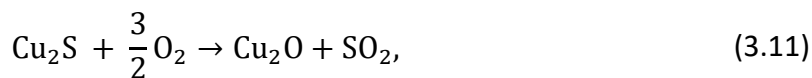
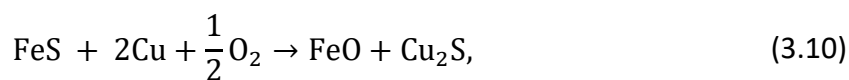
3.2.2 CONVERTING

In the converter, iron and sulfur are extracted from the matte, and a copper blister is produced. The feeding material consists mainly of matte from the flash furnace and silica sand, which is added to form the fayalite slag. In a Hoboken-type converter, the conversion is a batch process with two oxygen-enriched blows: slag blow and copper blow. The following steps can describe the process:

- 1) Loading with matte and silica sand.
- 2) **Slag blow**: removes iron from the metallic bath. This step avoids magnetite formation and leads to a fayalite slag (600 Nm³.h⁻¹, duration: about 2 h). Main reactions:



- 3) Slag tapping.
- 4) **Copper blow**: removes sulfur from the metallic bath. (1,500 Nm³.h⁻¹, duration: about 5h). Main reactions:



The SO_2 formed in these reactions can be used to produce H_2SO_4 .

5) Copper blister tapping.

The converter is the most critical equipment for the refractory wear due to its relatively high operating temperatures (up to 1400 °C), high $p\text{O}_2$ level, high Cu_2O content in the slag, and high thermal cycling. The most critical area in the converter is the tuyere zone ⁽¹⁾. This zone experiences an intense hot-face spalling due to high oxygen potential, thermal fluctuations, and a phenomenon so-called back-attack. The latter occurs when the blowing pressure cannot overcome the metallostatic pressure of the melt and the metal bath "returns" towards the tuyere wall. This wear mechanism leads to significant abrasion and is very common when the converter's charge is high. The campaign of the converter refractory lining (generally magnesia-chromite bricks) varies between 2 months (tuyeres) and 1.5 years (uptake shaft) ⁽¹⁶⁾.

3.2.3 REFINING

During refining, impurities (sulfur and oxygen) are eliminated from the copper blister through two stages: oxidation and reduction. The process generally involves the following steps:

- 1) Copper blister charging.
- 2) **Oxidation**: Eliminates the remaining sulfur from the copper blister by oxygen injection. Tuyeres are used to homogenize the bath with compressed air at gas

flow around $4 \text{ Nm}^3 \cdot \text{h}^{-1}$ and oxygen is blown through a lance. (Duration: about 2 h, depending on the sulfur content). Main reaction:



- 3) **Reduction**: Eliminates oxygen from the metallic bath by natural gas injection through the tuyeres. The CO generated by this reaction is directed to an incinerator to be transformed into CO_2 and released into the atmosphere. (Duration: around 2 h). Main reactions:



- 4) Copper anode tapping.

In the refining furnaces, there is no significant SO_2 concentration or matte corrosion. However, the slag has, in general, higher basicity and Cu_2O content than converter slags. Sodium is usually added to maximize the removal of impurities (As, Sb, Pb), leading to the corrosion of chromite in magnesia-chromite refractories to form sodium and chromium-containing compounds. These furnaces are often lined with magnesia-chromite bricks. However, alumina-chromia bricks have become an increasingly popular alternative. The campaign of refractories varies from 1 to 2 years in the tuyeres and body⁽¹⁶⁾.

3.2.4 ELECTROREFINING

Copper anodes are submitted to electrolytic refining with an acidified copper sulfate solution to produce copper cathodes (99.9 wt.% of purity). In this process, there is no significant refractory consumption⁽¹⁶⁾. The main reactions observed in this step are:

At the anode:



At the cathode:



3.3 FIRED MAGNESIA-BASED REFRACTORY BRICKS

Fired magnesia-based bricks are well known for their enhanced refractoriness and high resistance to chemically basic slags. They can be used in many different high-temperature industries and fall into four main categories: magnesia, magnesia-chromite, magnesia-spinel, and dolomite bricks.

3.3.1 MAGNESIA BRICKS

Bricks made from nearly 100 % pure magnesia-based raw materials, such as sintered MgO (dead burned magnesia – DBM), show MgO contents varying from around 90 % to about 98 %. Since pure MgO has a high melting point (2800 °C), the refractoriness of a magnesia-based brick is ultimately determined by the amount and type of impurity present within the grain ⁽¹⁷⁾. The generally observed impurities are CaO, SiO₂, Fe₂O₃, and B₂O₃. The lime to silica ratio (C/S) is a popular indicator of the refractoriness of magnesia bricks. Table III.4 gives the melting point of the main impurity phases formed according to different C/S ranges. For instance, when magnesia bricks are designed for the steel industry, the C/S ratio should be lower than 0.5 or higher than 1.5 to avoid the formation of monticellite and merwinite, which are liquid phases at the operating temperature (1500°C-1600°C). On the other hand, a high C/S ratio could promote the formation of low melting CaO-Fe₂O₃ phases. A phase diagram for the system CaO-MgO-SiO₂ at 1500 °C and 1 atm was calculated using the software FactSage™ (FToxid database) and is shown in Figure 3.4.

Magnesia bricks generally present a low thermal shock resistance due to the high thermal expansion coefficient of MgO. Their main application is as a permanent lining

in steelmaking, but they are also used in the non-ferrous, cement, lime, and glass industries.

Table III.4: Expected main phases formed for different molar CaO/ SiO₂ ratios in systems containing high MgO content.

| C/S ratio | Main phase | Chemical Formula | Melting point |
|-----------|---------------------|----------------------------|---------------|
| 0 – 0.5 | forsterite | 2MgO.SiO ₂ | 1750 °C |
| 0.5 – 0.9 | monticellite | CaO.MgO.SiO ₂ | 1450-1500 °C |
| 0.9 – 1.5 | merwinite | 2CaO.MgO.2SiO ₂ | ~1500 °C |
| 1.5 – 2.0 | dicalcium silicate | 2CaO.SiO ₂ | 1800-2000 °C |
| 2.0 – 3.0 | tricalcium silicate | 3CaO.SiO ₂ | >2000 °C |

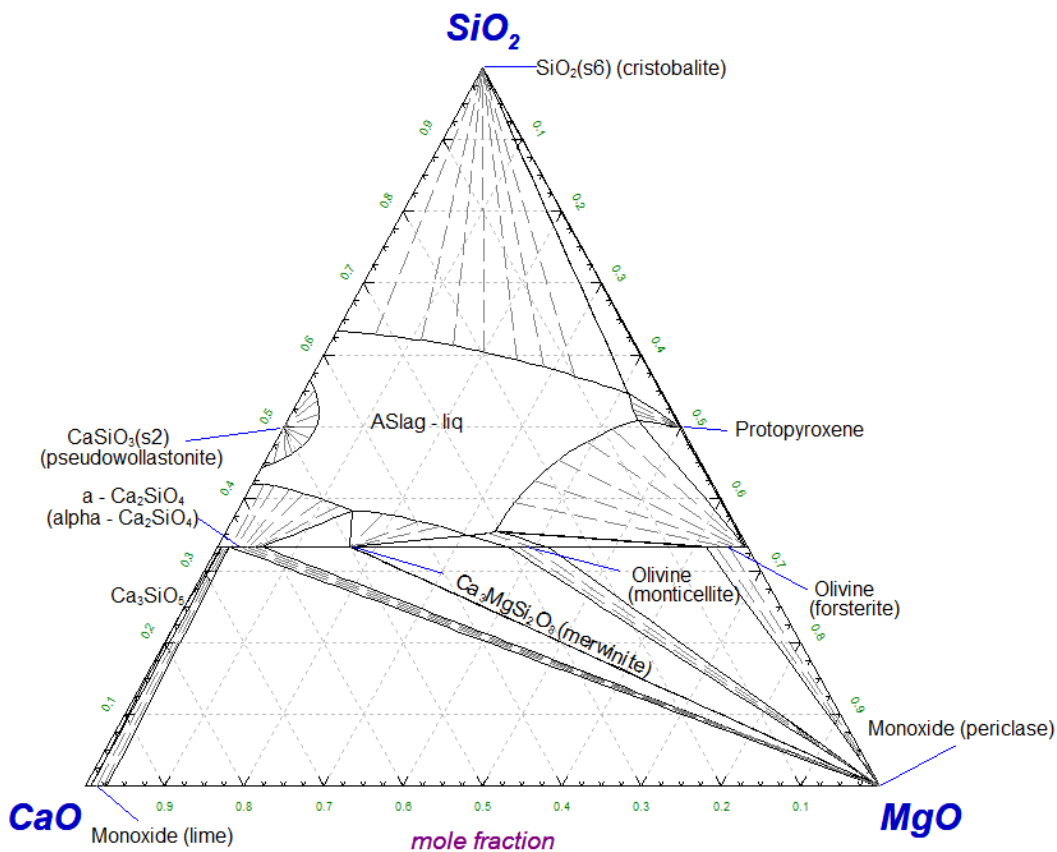


Figure 3.4: CaO-MgO-SiO₂ phase diagram (1500 °C and 1 atm) calculated in FactSage™.

Regenerator chambers in the glass industry use a variety of magnesia bricks. In the hot zone, where the waste gas is relatively clean (free from V₂O₅, alkali sulfates, SO₃, and sand carry-over), high purity fired magnesia bricks (≥ 97% MgO) are usually employed. The condensation zone is generally lined with forsterite-bonded magnesia-zircon

refractories due to the presence of gaseous SO_3 and the condensation of alkali sulfates. These bricks provide high corrosion resistance against sulfate attack under oxidizing conditions⁽¹⁸⁾.

3.3.2 MAGNESIA-CHROMITE BRICKS

Magnesia-chromite refractories are frequently used in the non-ferrous and steel industries due to their unique properties. The addition of chromite to magnesia refractories significantly increases its chemical resistance to low basicity slags and improves its thermal shock resistance. Several studies have shown that Cr_2O_3 and $\text{MgO} \cdot \text{Cr}_2\text{O}_3$ displays strong corrosion resistance to SiO_2 -based slags, such as $\text{CaO} \cdot \text{SiO}_2$ and $\text{FeO} \cdot \text{SiO}_2$ ⁽¹⁹⁾. Therefore, this class of refractories is still the best-seller for lining equipment such as RH degassers and copper converters despite environmental concerns.

Magnesia-chromite refractories are generally classified into three different classes: direct-bonded, rebonded, and semi-rebonded. Direct-bonded bricks are fired at temperatures above 1650 °C, and they have DBM and chromite as their primary raw materials, which are bonded through the formation of secondary spinel. Rebonded bricks are made from pre-reacted grains, mainly fused magnesia chromite or co-clinker (DBM and chromite sintered together), and are usually fired at higher temperatures (above 1700 °C). Semi-rebonded bricks contain all three raw materials: dead burned magnesia, chromite, and pre-reacted grains. A general comparison between the properties of these three classes is shown in Table III.5.

Table III.5: Overall comparison of the main properties of the different classes of magnesia-chromite bricks.

| Properties | Direct-bonded | Semi-rebonded | Rebonded |
|--------------------------|---------------|---------------|-----------|
| Thermal Shock Resistance | excellent | high | medium |
| Corrosion Resistance | medium | high | excellent |
| Abrasion Resistance | high | high | excellent |

3.3.3 MAGNESIA-SPINEL BRICKS

Although the term "spinel" is often used to describe the family of minerals that crystallize in the cubic system with a general formula $R'O.R''_2O_3$ ($R'=Mg$ or Fe ; $R''=Mg$, Fe , Al or Cr), magnesia-spinel bricks are known as MgO-based bricks containing mainly $MgO.Al_2O_3$ ⁽¹⁷⁾. The spinel contained in these bricks can be either added directly or formed in situ by alumina addition.

The main benefit of combining magnesia and spinel is the improved thermal shock resistance compared to pure magnesia bricks. This behavior is related to the microcracks caused during firing due to the different thermal expansion coefficients of magnesia and spinel. This leads to less spalling and longer refractory campaigns in many applications, such as in cement rotary kilns. The environmental pressure to use chrome-free magnesia-based bricks has increased magnesia-spinel bricks' popularity in the past decades ⁽¹⁷⁾.

3.3.4 DOLOMA BRICKS

Doloma-based bricks are composed mainly of calcined/sintered dolomite [$CaMg(CO_3)_2$], also known as doloma. Refractory-grade dolomites contain at least 20 wt.% MgO (42 wt.% $MgCO_3$) and a maximum of 2.5 wt.% impurities, such as silica, alumina, and iron ⁽²⁰⁾. High purity doloma bricks are equivalent to or even more refractory than magnesia bricks with up to 95% purity. Magnesia can be added to doloma bricks to improve its slag resistance in applications such as steel ladles and AOD vessels ⁽²⁰⁾. The main limitation of these bricks is their susceptibility to hydration. Their low resistance to acidic slags and gaseous sulfur oxides makes them unsuitable for use in the non-ferrous industry.

3.4 REFRACTORY TESTING

Refractory materials are generally characterized by their properties, which often determine their use and performance ⁽²⁰⁾. The most evaluated properties for refractory bricks are bulk density, apparent porosity, cold crushing strength, and chemical composition. Additional thermomechanical, chemical and microstructural properties can be assessed when further information is required.

3.4.1 BULK DENSITY AND APPARENT POROSITY

The bulk density (BD) of a refractory material is associated with its density, i.e. the mass of material within a unit volume ($\text{g}\cdot\text{cm}^{-3}$). The apparent porosity (AP) quantifies the presence of open pores on the surface of this material. AP is an important property for refractory materials since fluids such as molten charges, slag, and waste gases can fill these open pores and promote the refractory lining corrosion. Generally, a low apparent porosity is desired because it prevents the penetration of fluids into the refractory pore structure and increases the latter's corrosion resistance. BD and AP can be evaluated by measuring the masses of a sample in the dry, wet, and soaked in water. The filling of open pores with water can be conducted by applying a vacuum while the sample is soaked in water. If the refractory contains components that react with water, the same test can be performed using petrol-kerosene. Figure 3.5 illustrates the parameters needed to calculate BD and AP, where m_s is the mass of the dried specimen, m_u is the mass of the wet specimen (open pores filled with water), m_i is the mass of the refractory specimen when submerged in water, and V_{ap} is the specimen's apparent volume (true volume plus open and closed-pore volume).

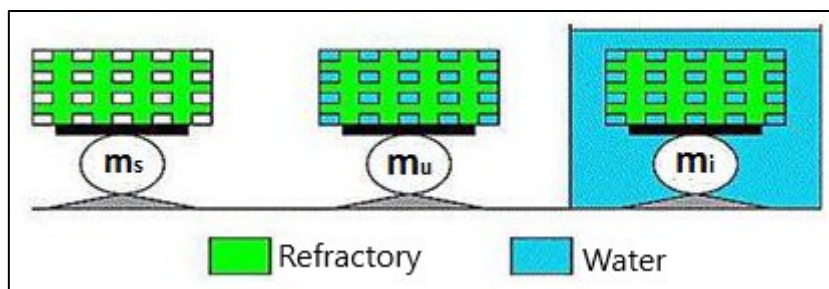


Figure 3.5: Parameters used for evaluating the bulk density and apparent porosity of refractory bricks.

BD and AP can be evaluated by Equations (2.20) to (2.22):

$$V_{\text{ap}} = \frac{m_u - m_i}{\rho_L} \quad (2.20)$$

$$\text{BD} = \frac{m_s}{V_{\text{ap}}} \quad (2.21)$$

$$\text{AP} = \frac{m_u - m_s}{\rho_L \times V_{\text{ap}}} \quad (2.22)$$

Although BD and AP are often inversely correlated, the former is greatly influenced by the refractory's chemical composition. In contrast, the latter is only affected by physical parameters, such as pressing conditions and firing temperature.

3.4.2 COLD CRUSHING STRENGTH

The cold crushing strength (CCS) of a refractory material indicates the strength of the grains and bonding system ⁽²⁰⁾. It is an important property to consider for refractory transportation, handling, and installation. In the cold crushing strength test (ASTM C-133), the refractory specimen collapses due to shear stresses related to an increasing load. CCS is evaluated considering the maximum load withstood by the specimen before its collapse.

3.4.3 X-RAY FLUORESCENCE SPECTROMETRY AND SULFUR ELEMENTAL ANALYSIS

X-ray fluorescence spectrometry (XRF) is an instrumental method of quantitative analysis for chemical elements. The working principle is based on measuring the

intensities of the X-ray spectral lines emitted by a secondary excitation ⁽²¹⁾. The applicability of XRF is nearly unlimited in terms of the type of sample and concentration range. However, the appropriate testing and sample preparation techniques should be chosen according to the nature of a given sample. In the case of refractory materials, the samples are previously fused using lithium tetraborate ($\text{Li}_2\text{B}_4\text{O}_7$), and a predetermined program is used for testing. The test's outcome is the amount of each of the following oxides contained in the specimen: Na_2O , MgO , Al_2O_3 , SiO_2 , P_2O_5 , SO_3 , K_2O , CaO , TiO_2 , Cr_2O_3 , MnO , Fe_2O_3 , ZrO_2 , BaO , and HfO_2 .

Sulfur elemental analysis can be performed as a more reliable test to determine the amount of S (or calculated SO_3) in the refractory sample. The sample is previously digested in a high-frequency induction furnace, and the resulting gas is then captured and evaluated by infrared adsorption. International standards are used for testing according to the sulfur concentration range of the analytical sample.

3.4.4 X-RAY DIFFRACTION

X-ray diffraction (XRD) is a powerful technique used for characterizing crystalline materials. This method provides information regarding the structural parameters of the tested specimen through the analysis of its X-ray diffraction lines. These lines are generated through the constructive interference of a monochromatic beam of X-rays scattered at specific angles from each set of lattice planes in a sample ⁽²²⁾. The X-ray diffraction pattern produced by this technique can be considered a fingerprint of the atomic arrangements in a sample. Comparison with a standard database enables phase identification of the crystalline material ⁽²²⁾.

3.4.5 CORROSION OF BASIC REFRACTORIES BY SULFUR GASES

The oxidation of sulfidic ores used in primary non-ferrous metal production leads to a significant amount of SO_2 gas in the reaction vessel. The equilibrium reaction regarding the conversion of SO_2 to SO_3 (equation 2.2) is slowed down above 760°C . Nevertheless, a relevant SO_3 partial pressure in the furnace can be assumed to exist in

the temperature range of 760-1100 °C ^(23; 8). The sulfur gases in the furnace atmosphere penetrate the magnesia brick's pores and react with the basic oxides below 1050 °C to form alkaline earth sulfates ⁽¹⁾:



The sulfur content is usually higher in the refractory's cold face, where the temperature during operation generally does not exceed 1050 °C. Equations 2.23 and 2.24 are accompanied by a theoretical volume increase of 290% and 250%, respectively, which causes the brick pores' filling-up. The consequent densification of the refractory section promotes the formation of cracks upon temperature fluctuations, which makes the brick susceptible to melt infiltration and accelerates the wear of the refractory lining ⁽¹⁾. When the temperature in this brick section increases due to the advancing interface with the bath material, MgSO_4 dissociates to fine crystalline MgO , leaving a weak bond structure behind ⁽²³⁾. A schematic representation of this wear mechanism is shown in Figure 3.6.

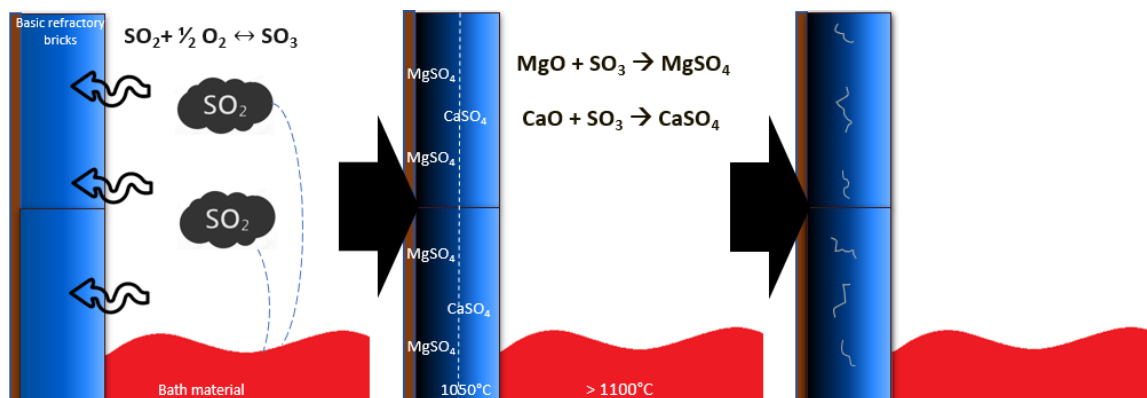


Figure 3.6: Schematic representation of the corrosion of basic refractories by sulfur gases during copper smelting.

Many factors determine the intensity of sulfate corrosion, such as the amount of supplied SO_2 , the brick's properties (porosity, chemical composition, type of bonding, etc.), and the reaction temperature and time ⁽²³⁾. A high CaO/SiO_2 ratio in the brick

leads to the corrosion of the interstitial phase C_2S to form $CaSO_4$ according to the following equation ⁽²³⁾:



This promotes a continuous decrease in the CaO/SiO_2 ratio, resulting in forsterite crystals close to the brick's hot face. According to Malfliet *et al.* ⁽¹⁾, the most common phases found in magnesia bricks can be ordered according to their increasing resistance to sulfur gas attack in the following manner: $MgO < C_2S (Ca_2SiO_4) < C_3MS_2(Ca_3MgSi_2O_8) < CMS (CaMgSiO_4) < M_2S (Mg_2SiO_4) < (Mg,Fe)(Cr,Al,Fe)_2O_4$.

4. MATERIALS AND METHODS

4.1 SAMPLE PREPARATION AND SELECTION

Eight refractory formulations were prepared at the Research and Development Center of RHI Magnesita in Leoben (Austria). Seven magnesia bricks were produced with different CaO/SiO₂ (C/S) ratios, and an alumina brick was prepared for reference purposes. All magnesia bricks were produced using dead burned magnesia (DBM) grains from Turkey with a grain bulk density of 3.42 g.cm⁻³ and a CaO content of 1.9 wt.% and magnesium-based lignosulfonate as a binder. The total impurity content in the sintered magnesia, such as SiO₂ and Fe₂O₃, is about 1 wt.%. Undensified microsilica (98.4 wt.% SiO₂) was added to the recipes in different amounts to vary the C/S ratio (Table IV.1). All recipes were produced with the same grain size distribution from 5.0 mm to 50 μm, mixed in an intensive lab-scale Eirich mixer for 4 min, and pressed at 170 MPa using a hydraulic press. The grain size distribution of the brick fines (< 50 μm) varied due to the addition of microsilica. The reference composition (sample RS) was produced with 100% tabular alumina and grain size distribution similar to the magnesia bricks.

Table IV.1: Refractory compositions used in this study and their calculated C/S ratios

| Composition | DBM (%) | Microsilica (%) | Calc. C/S total | Calc. C/S matrix |
|-------------|---------|-----------------|-----------------|------------------|
| C0 | 100.0 | 0.0 | 2.90 | 2.90 |
| C1 | 99.8 | 0.2 | 2.26 | 1.82 |
| C2 | 99.5 | 0.5 | 1.69 | 1.16 |
| C3 | 99.0 | 1.0 | 1.19 | 0.72 |
| C4 | 98.2 | 1.8 | 0.80 | 0.44 |
| C5 | 96.5 | 3.5 | 0.47 | 0.24 |
| C6 | 94.0 | 6.0 | 0.29 | 0.16 |

Different C/S ratios lead to distinct amounts of liquid phase formed in each brick during firing, which in turn affects the sintering degree of the microstructure and, thus, the brick's properties. Therefore, FactSageTM calculations were performed to determine the optimal firing temperatures. Each mixture gave rise to 12 bricks, which

were then air-dried at 150 °C for 12 h. These samples were subsequently divided into three groups and heat-treated in air for 12 h at 1450, 1550, or 1630 °C. The temperature range of 1450-1630 °C was selected to conduct the sintering step because the difference in the volume of the liquid phase formed within this range is substantial. Moreover, this temperature range is commonly used in the firing of several commercially available magnesia-based refractories. After firing, the bricks were examined to determine their BD, AP, and CCS. Archimedes tests evaluated the apparent porosity (AP) and bulk density (BD) according to DIN EN 993-1. The cold crushing strength (CCS) of the as-prepared samples was evaluated at room temperature with a FORM+TEST MEGA 10 600 kN press. These tests were carried out based on DIN EN 993-5. Mercury intrusion porosimetry (MIP) and chemical analyses through XRF and XRD were performed to elucidate the difference in the brick's properties after firing at each temperature. X-ray diffraction (XRD) was conducted on a Bruker D8 Advance diffractometer using Cu K α ($\lambda = 1.54 \text{ \AA}$) as the radiation source. X-ray fluorescence spectrometry (XRF) was carried out with a Bruker S8 Tiger system, employing RhK α as an exciting source. Mercury intrusion porosimetry (MIP) was conducted at room temperature on a Micromeritics Poresizer 9500 porosimeter.

Corrosion tests were performed mainly to determine the influence of the C/S ratio on the specimens' corrosion resistance. Parallely, the influence of the specimens' porosity was also evaluated. Thus, three corrosion tests were performed as described in Table IV.2.

Table IV.2: Corrosion tests conducted in this study and their objectives.

| Corrosion test | Objective | Number of specimens from each composition | Number of repetitions |
|-----------------------|---|--|------------------------------|
| I | Influence of the C/S ratio | 1 | 4 |
| II | Influence of porosity | 2-3 | 1 |
| III | The combined effect of porosity and C/S ratio | 2 | 1 |

For the corrosion test I, the firing temperature of each sample was selected based on the bricks' porosity to minimize the influence of this property. Based on the results in

Figure 5.2, the porosity of the basic bricks was fixed at (13.7 ± 0.3) % and the following firing temperatures were selected for each composition:

- 1450 °C: C3, C4, and C5.
- 1550 °C: C2.
- 1630 °C: C0, C1, C6, and RS.

In corrosion test II, the sample C5 was chosen due to its considerable porosity variation as a firing temperature function. In this case, the chemical composition was kept constant, and the variation in physical properties was evaluated.

The combined effect of firing temperature/porosity and C/S ratio was evaluated in the corrosion test III. Samples C0 and C6 (maximum and minimum C/S ratios, respectively) fired at 1450, and 1630 °C were selected for this test.

4.2 CORROSION RESISTANCE

4.2.1 TESTING PROCEDURE

The novel test was performed according to the procedure described below and illustrated in Figure 4.1:

1. A box (20x25x10 cm, wall thickness of 4 cm) was initially prepared using an alumina-based refractory brick. Its bottom portion was covered with about 260 g of fine aluminum sulfate ($D_{50} = 0.3\text{mm}$, $\text{SO}_3 = 39\%$).
2. Each refractory brick tested in this study was cut into cube-shaped samples with an edge length of 30 mm. The cubes were previously weighted.
3. Two cubes were examined to determine BD and AP using petrol-kerosene. These tests provided information concerning the original properties of each formulation prepared in this study.
4. Eight cube-shaped samples of different refractory bricks were positioned inside the box on an alumina-based refractory plate to avoid direct contact between the cubes and aluminum sulfate.

5. The box was closed using an alumina-based insulating blanket (3mm thickness, withstands up to 1260°C) and a lid made of the same material as the box (Figure 4.2). Bricks (amounting to approx. 10kg) were placed on top of the lid to apply pressure and limit the gas flow out of the box. The system was heat-treated in air at 900 °C for 12 h at a heating rate of 100 °C.h⁻¹ (Figure 4.3).

6. After the test, BD and AP were evaluated for each cube. The cubes were subsequently air-dried at 120 °C for 6 h and then examined by XRF, elemental sulfur analysis (DIN 51085:2015-01), and XRD. Moreover, the aluminum sulfate concentration was determined after the corrosion test by elemental sulfur analysis aiming to evaluate its decomposition. Optical microscopy images were also taken from selected specimens.

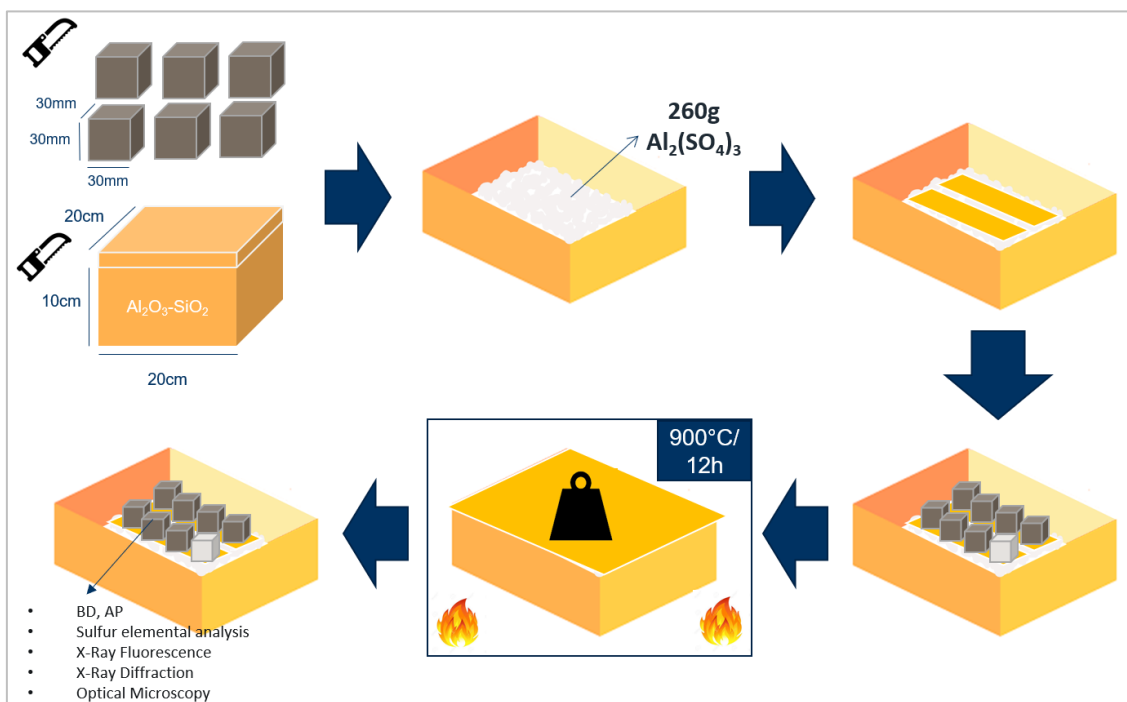


Figure 4.1: Schematic diagram of the test procedure

Aluminum sulfate was used in this test due to its low stability and lower decomposition temperature than magnesium sulfate. The testing temperature was selected in an interval between the decomposition temperatures estimated for $\text{Al}_2(\text{SO}_4)_3$ and MgSO_4 , as shown in Figure 4.4. In this temperature range, aluminum sulfate decomposes into SO_3 , reacting with the refractory specimen to form MgSO_4 and CaSO_4 .

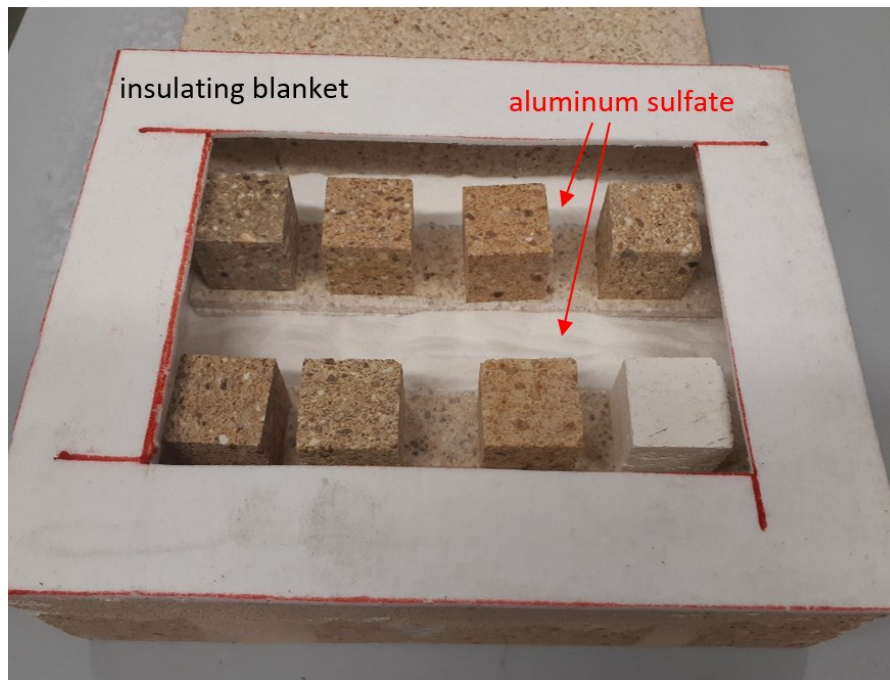


Figure 4.2: Setup used in the corrosion tests



Figure 4.3: Closed box containing the sample bricks and positioned inside a furnace.

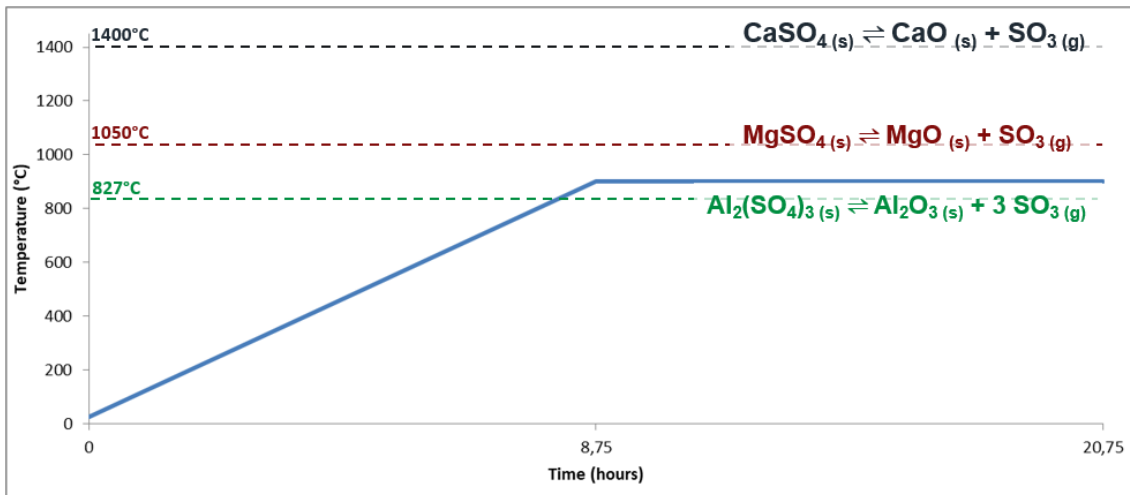


Figure 4.4: Test temperature (solid line) and final decomposition temperatures estimated for $\text{Al}_2(\text{SO}_4)_3$, MgSO_4 , and CaSO_4 (dashed lines).

4.2.2 QUANTITATIVE ANALYSIS

As in 4.1, the apparent porosity (AP) and bulk density (BD) of the samples after the corrosion tests were evaluated by Archimedes tests according to DIN EN 993-1. The corroded samples were examined using petrol-kerosene instead of water due to the high solubility of sulfates in the latter. The values obtained for AP and BD before and after the exposure of samples to SO_2 and SO_3 were used for evaluating their corrosion resistance. These analyses were conducted using Equations (4.1) and (4.2):

$$\Delta\text{BD} (\%) = \frac{\text{BD}_{\text{after}} - \text{BD}_{\text{before}}}{\text{BD}_{\text{before}}} \times 100\% \quad (4.1)$$

$$\Delta\text{AP} (\%) = \frac{\text{AP}_{\text{before}} - \text{AP}_{\text{after}}}{\text{AP}_{\text{before}}} \times 100\% \quad (4.2)$$

The sulfur concentration in the examined materials was determined in a Leco CS 200 / 230 apparatus following the recommendations of DIN 51085. The larger the variation in BD (ΔBD) and AP (ΔAP) and the higher the sulfur content, the lower the sample's corrosion resistance. This behavior is related to the fact that materials with a high

deviation in these values exhibit a pronounced blocking of pores due to the infiltration of sulfur gases and the formation of MgSO_4 and CaSO_4 (Equations 2.23 and 2.24).

The statistical significance of the obtained results was evaluated by one-way analysis of variance (ANOVA) and post hoc Fisher's protected least significant differences (LSD) multiple comparison test (corrosion test I) and repeated measures ANOVA (corrosion test II). The absolute values (modules) of ΔBD and ΔAP were considered in these analyses. The significance level (α) was fixed at 0.05.

4.2.3 QUALITATIVE ANALYSIS

The presence of magnesium sulfate, calcium sulfate, and sulfate hydrates was detected by XRD [Bruker D8 Advance diffractometer using $\text{Cu K}\alpha$ ($\lambda = 1.54 \text{ \AA}$) as the radiation source]. Reflected light optical microscopy (OM) was performed on polished sections. Scanning electron microscopy (SEM) was performed on selected samples using a JEOL JSM-6460 at an accelerating voltage of 20 kV. The samples examined by SEM were previously sputter-coated with a thin carbon layer. The images were examined and compared to micrographs of previous post-mortem studies in which the corrosion of refractory bricks by sulfur gases was considered as an important wear factor, such as Figures 1.3, 1.4 and 1.6.

5. RESULTS AND DISCUSSION

Table V.1 gives the chemical composition obtained by XRF for the materials prepared in this work. As was expected, MgO is the dominant phase in C0 to C6, while Al₂O₃ mainly forms RS. The same result was also obtained by XRD. The C/S ratios shown in Table V.1 are similar to those described in Table IV.1. This finding means that the ratios theoretically calculated match with those experimentally determined by XRF.

Table V.1: Chemical composition obtained by XRF for the materials fabricated in this study. Examinations conducted on as-prepared samples (before corrosion tests).

| Sample | Chemical composition (wt.%) | | | | | | C/S ratio | Calc. C/S ratio ⁽²⁾ |
|-----------|-----------------------------|-----|------------------|--------------------------------|--------------------------------|----------------------|-----------|--------------------------------|
| | MgO | CaO | SiO ₂ | Al ₂ O ₃ | Fe ₂ O ₃ | Other ⁽¹⁾ | | |
| C0 | 96.7 | 2.0 | 0.8 | 0.2 | 0.2 | 0.1 | 2.5 | 2.90 |
| C1 | 96.5 | 2.0 | 1.0 | 0.1 | 0.2 | 0.2 | 2.0 | 2.26 |
| C2 | 95.9 | 2.1 | 1.4 | 0.2 | 0.2 | 0.2 | 1.5 | 1.69 |
| C3 | 95.8 | 2.0 | 1.8 | 0.1 | 0.2 | 0.1 | 1.1 | 1.19 |
| C4 | 95.1 | 2.0 | 2.5 | 0.1 | 0.2 | 0.1 | 0.8 | 0.80 |
| C5 | 93.6 | 1.9 | 4.1 | 0.1 | 0.2 | 0.1 | 0.5 | 0.47 |
| C6 | 90.5 | 2.1 | 7.0 | 0.1 | 0.2 | 0.1 | 0.3 | 0.29 |
| RS | 0.4 | – | 0.1 | 99.2 | 0.1 | 0.2 | 0.0 | - |

⁽¹⁾ Associated with phases such as SO₃, P₂O₅, MnO, and Na₂O.

⁽²⁾ Calculated C/S ratio shown in Table IV.1 for comparison.

The FactSage™ software was employed to evaluate the volume of the liquid phase formed during sintering. Temperatures from 1450 to 1630 °C at a step size of 20 °C were considered in these calculations. The obtained curves are displayed in Figure 5.1. The increase in the sintering temperature generally leads to larger volumes of the liquid phase. It is well established that densification is more effective when sintering occurs in the presence of a liquid phase because both the atomic diffusion and interparticle bonding are favored under this condition ⁽²⁴⁾ ⁽²⁵⁾. This behavior is particularly noticed for samples containing C/S ratios between 0.3 and 1.7 (C6, C5, C4, C3 and C2), due to the presence of monticellite and merwinite as the interstitial

phases. C5 shows the most significant increase in the amount of liquid phase with increasing temperature due to its high amount of silica (4.1%) and the fact that merwinite is its main secondary phase (melting temperature: 1450-1500°C). Although C6 has a higher amount of silica than C5, its main secondary phase is forsterite, which has a higher melting point (above 1630°C).

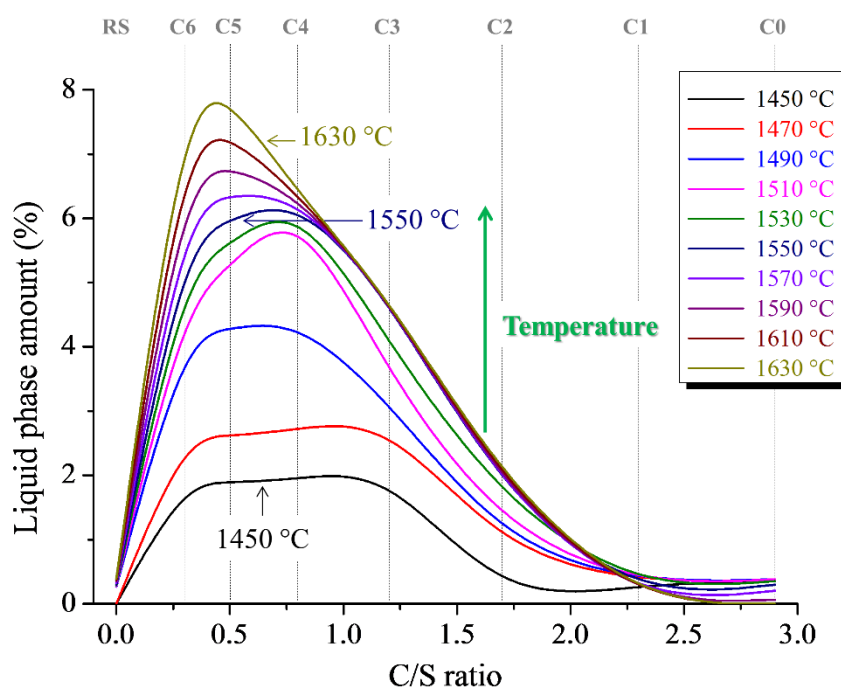


Figure 5.1: Simulation performed on the FactSageTM software to evaluate the liquid phase volume formed in different samples at temperatures ranging from 1450 to 1630 °C.

Figure 5.2 depicts AP and CCS as a function of both the C/S ratio and sintering temperature. It can be noted that AP is reduced, and CCS becomes larger when the sintering temperature is increased. This behavior is associated with more effective sintering when the heat treatment temperature is raised, which causes the elimination of pores and an increase in the samples' mechanical strength⁽²⁶⁾. The inset displayed in Figure 5.2: AP and CCS as a function of the C/S ratio and sintering temperature. The dashed lines are used only as a guide for the eyes. Inset: pore size distribution of sample C0 sintered in air at 1450, 1550, and 1630 °C. The highlighted value (13.7 %) was used as a reference in the selection of the samples used in corrosion test I. exhibits a

representative pore size distribution obtained by MIP for a specimen heat-treated at 1450, 1550, or 1630 °C. One observes that the increase of the sintering temperature shifted the distribution towards larger pores. Indeed, the mean pore size evaluated for this sample when sintered at 1450, 1550, and 1630 °C was 4, 8, and 11 μm , respectively. This behavior is related to the closure of small pores as sintering progresses, promoting the densification of the pore structure and a decrease in AP ⁽²⁶⁾. It can also be noted that AP and CCS are generally inversely proportional. It is well known that pores in ceramic materials adversely affect their mechanical stability; since ceramics are fragile, such defects can act as stress concentrators and decrease their strength ⁽²⁷⁾.

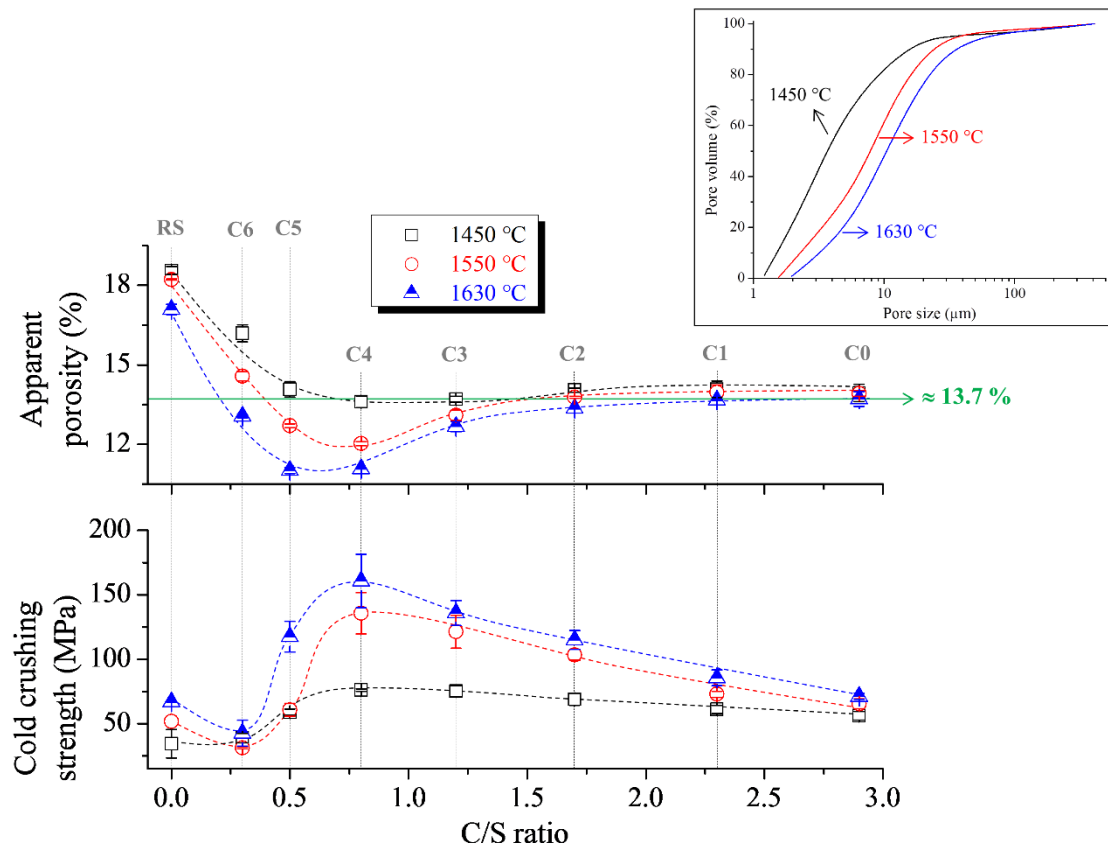


Figure 5.2: AP and CCS as a function of the C/S ratio and sintering temperature. The dashed lines are used only as a guide for the eyes. Inset: pore size distribution of sample C0 sintered in air at 1450, 1550, and 1630 °C. The highlighted value (13.7 %) was used as a reference in the selection of the samples used in corrosion test I.

5.3 CORROSION TEST I

Aiming to minimize the influence of AP on the corrosion tests, samples with porosity as close as possible to 13.7 % were used in these examinations (this value is highlighted in Figure 5.2). As a result, the following sintering temperatures were selected for each composition: 1450 °C (C3, C4, and C5), 1550 °C (C2), and 1630 °C (C0, C1, C6, and RS). It is worth mentioning that sample RS showed porosity around 17 % even when heat-treated at 1630 °C, which is higher than the value used as the reference in the corrosion tests. Nonetheless, this sample was used as a standard in these tests despite its large porosity. The visual aspect of the samples after the corrosion test I is shown in Figure 5.3. No significant difference could be observed in the cubes before and after the test.



Figure 5.3: Visual aspect of the refractory samples after corrosion test I

Figure 5.4 depicts AP and BD variation for samples used in the corrosion tests (Equations 4.1 and 4.2). The SO_3 concentration in the examined specimens is also shown. Samples with C/S ratios above 0.5 displayed similar ΔAP and ΔBD (from C5 to C0). Sample RS exhibited the smallest variation in AP and BD, followed by C6. Interestingly, BD followed a trend similar to sulfur concentration when examined according to the C/S ratio. This result reveals that the higher the amount of sulfur in

the tested sample, the smaller its porosity and the larger its density. This finding is related to the blocking of pores due to the formation of sulfates in the refractory structure (Equations 2.23 to 2.25). The concentration of SO_3 in sample RS was negligible, which agrees with the low variation in AP and BD displayed by this material. As shown in Figure 4.4, $\text{Al}_2(\text{SO}_4)_3$ decomposes at temperatures around 800 °C, indicating that the reaction of sulfur gases with alumina-based materials should not give rise to aluminum sulfate at 900 °C. The small values of ΔAP and ΔBD evaluated for sample RS also reveal no noticeable structural change due to its heating during the corrosion test. Therefore, the variation in AP and BD observed for the examined samples is strongly related to sulfur penetration into the pore structures and is not associated with the occurrence of additional structural changes due to heat treatment (e.g., pore closure).

Table V.2 exhibits the results obtained by one-way ANOVA. This test revealed a statistically significant difference among the tested samples for all dependent variables considered in the corrosion test (AP, BD, and sulfur content). As the obtained p-values are smaller than 0.05, we can assume that at least one of the group means is significantly different from the other ones, and it is valid to proceed with the post hoc testing⁽²⁸⁾. Table V.3 shows the results obtained by Fisher's Protected LSD tests. These results indicate that C6 was significantly different from the other samples regarding all three properties. C5 showed a statistical difference in BD when compared to C1 and C2. The same cannot be stated for the other properties. Therefore, it can be noted that recipe C6 displayed higher resistance to sulfur gases than the other magnesia-based recipes. However, it cannot be concluded that the higher the silica content in the sample (and the lower the C/S ratio), the higher the resistance to SO_2/SO_3 .

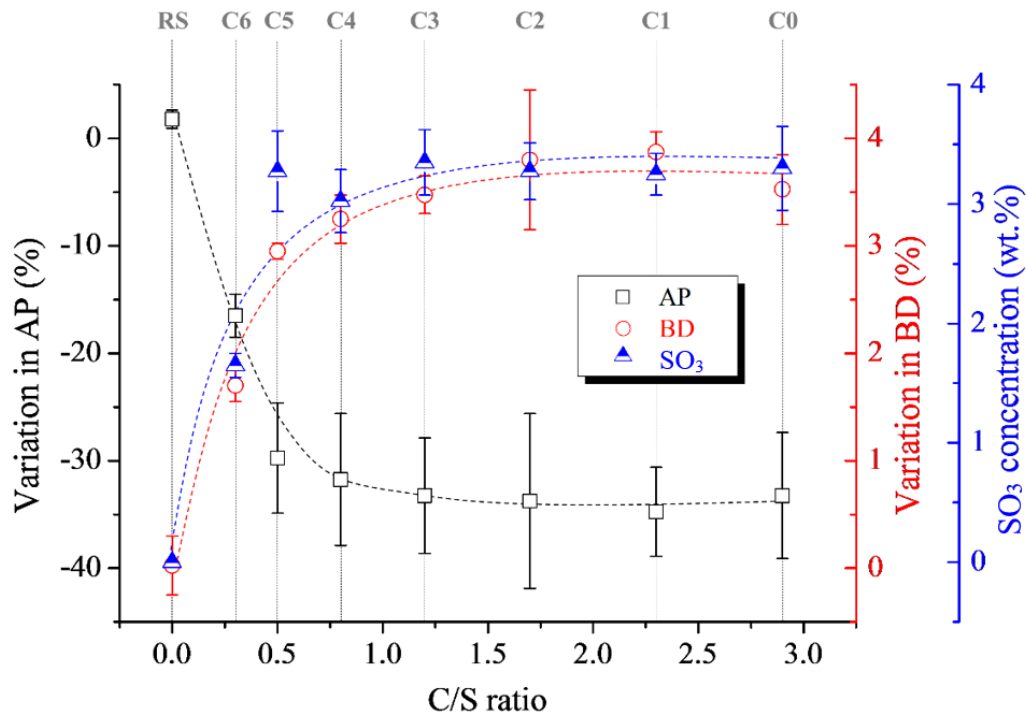


Figure 5.4: Variation in AP and BD as a function of the C/S ratio evaluated considering the values obtained before and after the corrosion tests (Equations 4.1 and 4.2). The SO_3 concentration in the tested materials is also shown.

Table V.2: F ratios and p-values obtained by one-way ANOVA to compare samples C0 to C6 regarding the following properties: change in bulk density, change in apparent porosity, and sulfur content.

| | ΔBD ($\text{g}\cdot\text{cm}^{-3}$) | ΔAP (%) | Sulfur content (wt.%) |
|---------|---|-----------------------|-----------------------|
| F ratio | 11.608 | 2.948 | 12.026 |
| p-value | 0.0001 | 0.030 | 0.0001 |

Table V.3: p-values obtained by Fisher's Protected LSD test to compare samples C0 to C6 regarding the following properties: change in bulk density, change in apparent porosity, and sulfur content.

| | | Δ BD | Δ AP | Sulfur content |
|----|-----|-------------|-------------|----------------|
| | Vs. | p-value | p-value | p-value |
| C6 | C5 | 0.0006* | 0.0181* | 0.0001* |
| | C4 | 0.0001* | 0.0083* | 0.0001* |
| | C3 | 0.0001* | 0.0043* | 0.0001* |
| | C0 | 0.0001* | 0.0041* | 0.0001* |
| | C2 | 0.0001* | 0.0032* | 0.0001* |
| | C1 | 0.0001* | 0.0023* | 0.0001* |
| C5 | C4 | 0.3564 | 0.7305 | 0.391 |
| | C3 | 0.0982 | 0.5317 | 0.3497 |
| | C0 | 0.0779 | 0.5196 | 0.2764 |
| | C2 | 0.011* | 0.4528 | 0.2639 |
| | C1 | 0.0068* | 0.3764 | 0.2184 |
| C4 | C3 | 0.4399 | 0.777 | 0.9366 |
| | C0 | 0.373 | 0.7626 | 0.8114 |
| | C2 | 0.0792 | 0.6817 | 0.7884 |
| | C1 | 0.0522 | 0.585 | 0.6985 |
| C3 | C0 | 0.9033 | 0.9849 | 0.8736 |
| | C2 | 0.3021 | 0.8985 | 0.8501 |
| | C1 | 0.2176 | 0.7915 | 0.758 |
| C0 | C2 | 0.3605 | 0.9135 | 0.9762 |
| | C1 | 0.2638 | 0.8061 | 0.8814 |
| C2 | C1 | 0.8332 | 0.891 | 0.905 |

*Values $p < 0.05$ indicate that the groups are statistically different.

The weight variation of each cube and the whole box was determined after two out of the four test repetitions. The weight increase of the samples was in line with the Δ BD results in Figure 5.4: similar results for samples C0-C5 ($3.3 \pm 0.1\%$), about 50% lower values for sample C6 ($1.6 \pm 0.2\%$) and negligible change for sample RS ($-0.06 \pm 0.00\%$). The sum of the samples' weight increased 18.2 ± 0.6 g after the test due to the formation of sulfates, and the whole box had a weight decrease of 199.1 ± 0.8 g. Mass balance calculations show that 260g of aluminium sulfate would give rise to 182.5 g $\text{SO}_{3(g)}$ after complete decomposition, which would partially react with the samples and

partially be released in the furnace atmosphere. This means a maximum of 164.3g (182.5g - 18.2g) total weight loss can be attributed to non-reacted $\text{SO}_{3(g)}$ release. The remaining 35.1g could be associated with other factors, such as changes in the insulating blanket during firing. After the test, the aluminum sulfate's residual SO_3 content was $2.26 \pm 0.05\%$, much lower than the 39% present in the original material. These results confirm that the test temperature and duration were enough to decompose most of the aluminum sulfate inside the box and create a sulfur rich atmosphere that would lead to the corrosion of basic brick samples.

Figure 5.5 shows XRD patterns of C0 to C6 after the corrosion tests. One observes that magnesium sulfate (main reflection lines labeled with asterisks) was detected in considerable amounts in these materials, especially in C0 to C5. Forsterite (main peaks marked with arrows) was detected in C6, C5, and C4, but at a larger concentration in C6. As discussed before, forsterite has been reported to have high chemical resistance to the attack of sulfur gases⁽²⁹⁾. Figure 5.6 depicts XRD patterns of C0 and C6 before (as-prepared) and after the corrosion tests. Forsterite was detected at a significant proportion in C6, but it was not observed in C0. Due to its low silica content and high C/S ratio, the main interstitial phase detected in C0 was Larnite. Magnesium sulfate peaks were visible in the C0 XRD pattern after the corrosion test and almost imperceptible in the C6 pattern. As discussed earlier, C0 has low corrosion resistance, while C6 was the MgO-based formulation least affected by the chemical attack of sulfur gases. This behavior seems to be closely related to the presence of forsterite in C6. It was estimated from a refinement procedure applied to the XRD pattern of C6 that the forsterite concentration in this material was as high as 10 wt.%.

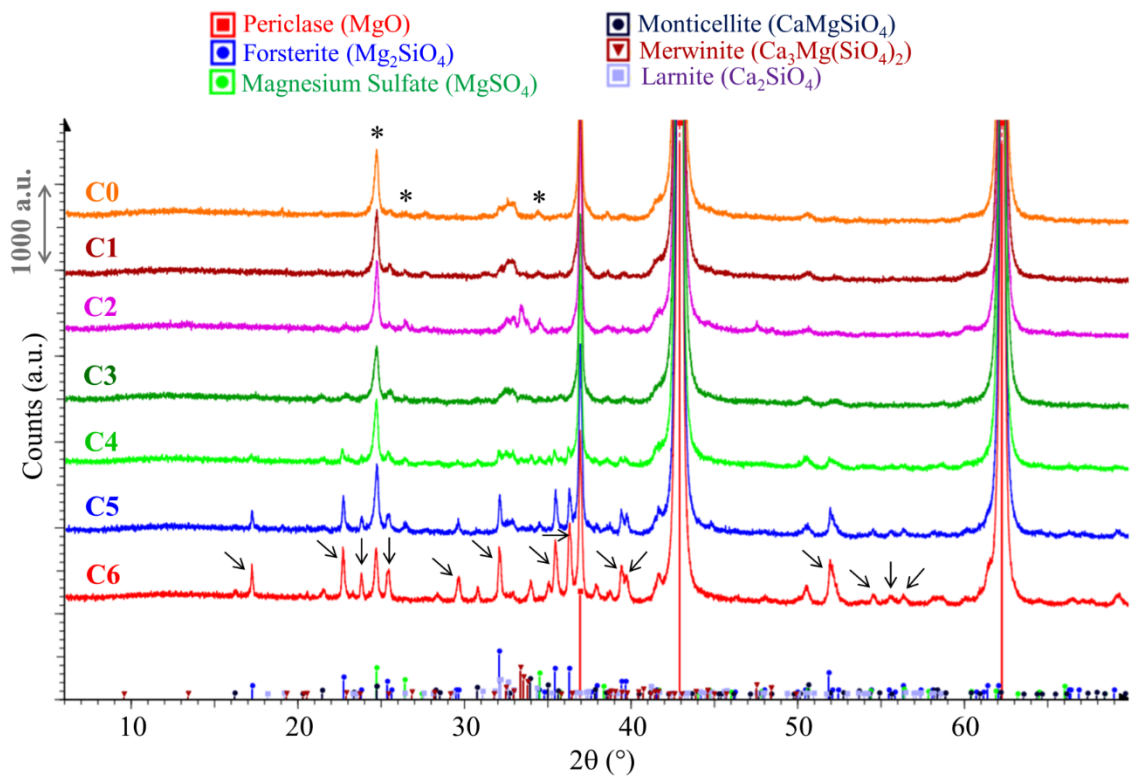


Figure 5.5: XRD patterns of samples C0 to C6 after the corrosion test. The main peaks associated with MgSO_4 and Mg_2SiO_4 were labeled with asterisks and arrows, respectively

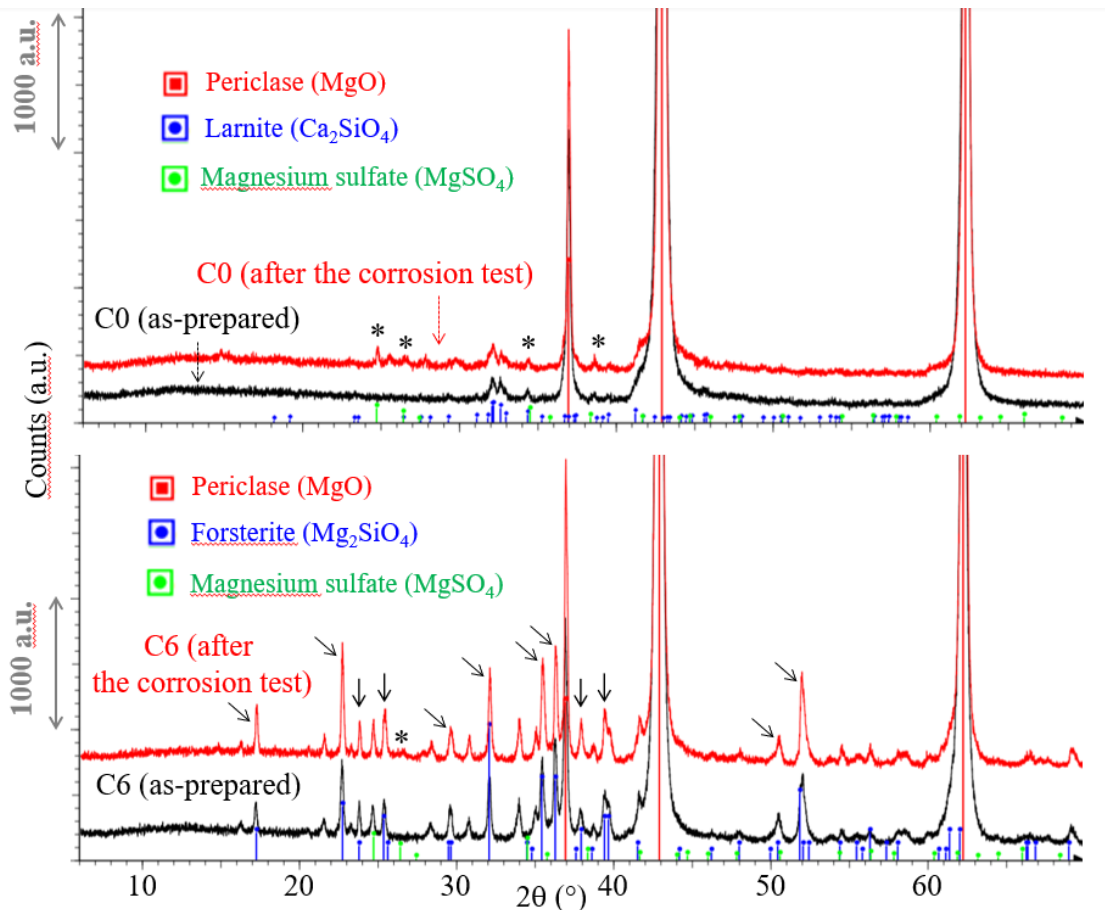


Figure 5.6: XRD patterns of C0 and C6 before (as-prepared) and after the corrosion test. The main peaks associated with MgSO_4 and Mg_2SiO_4 were labeled with asterisks and arrows, respectively.

Figure 5.7 displays OM micrographs of C0 and C6. The microstructures of C6 before (as-prepared) and after the corrosion test are similar, indicating that this material withstood the chemical attack from sulfur gases and showed no significant structural change. A high amount of forsterite is observed in the microstructure of C6, which is in agreement with the XRD results. The forsterite surrounding the MgO grains may have acted as a barrier to grain corrosion. On the other hand, Mg_2SO_4 was noticed surrounding the MgO grains in C0, revealing that this material experienced corrosion during the test.

Figure 5.8 exhibits backscattered electron SEM images of C0. A thick Mg_2SO_4 layer is observed on the MgO grains after the corrosion test. Ca_2SiO_4 is also noticed in this material, which was also detected by XRD (Figure 5.6). The images of C0 after the

corrosion test in Figures 5.7 and 5.8 show some resemblance to OM and SEM images obtained in previous post-mortem studies, such as Figures 1.3 and 1.6.

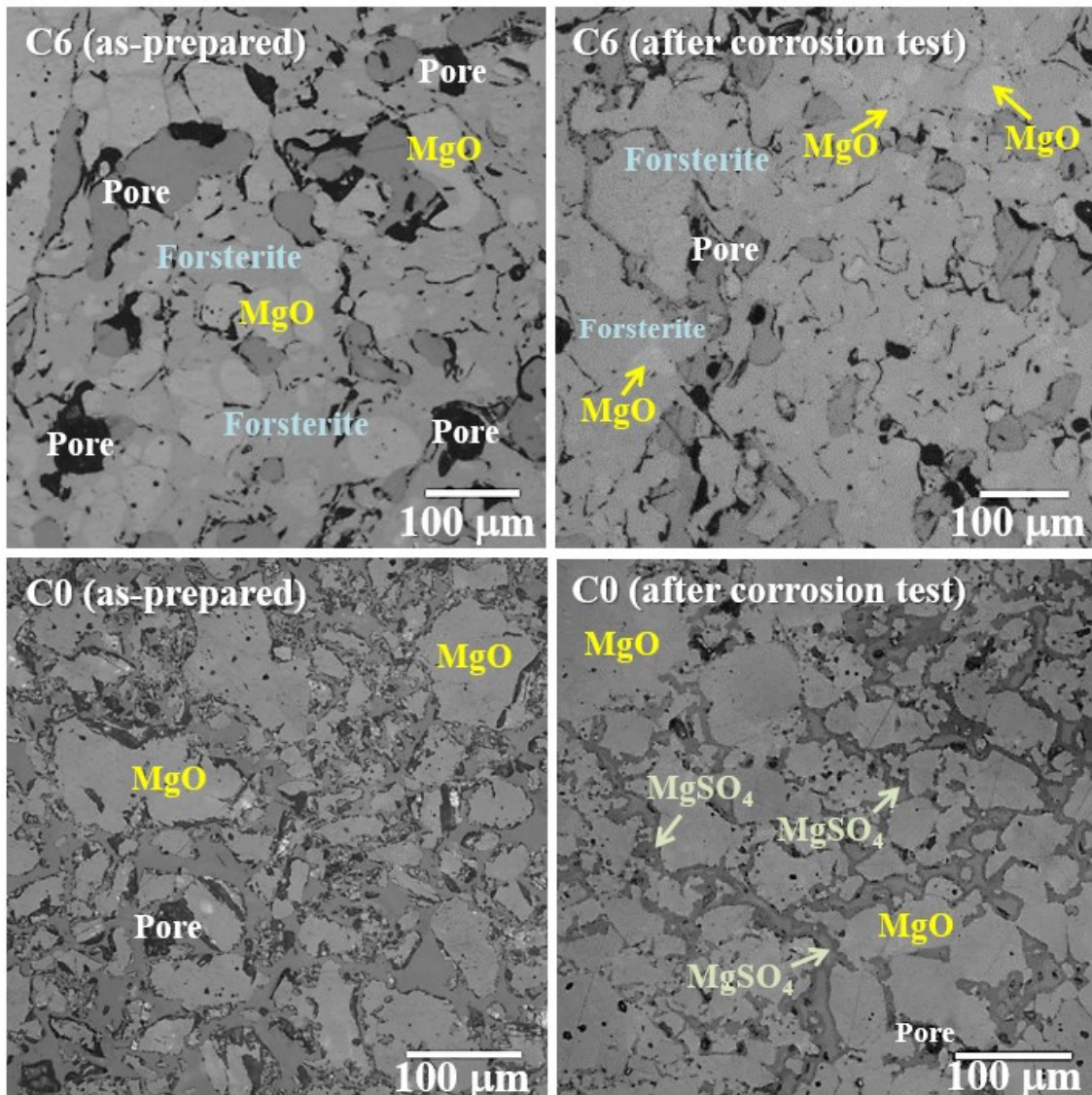


Figure 5.7: OM micrographs of C0 and C6 before (as-prepared) and after the corrosion tests. The presence of MgSO₄ is indicated on the DBM grains in C0 after the corrosion test.

Based on the results from corrosion test I, it is recommended to use forsterite containing magnesia-based refractories (ensure C/S ratio ≤ 0.3) in regions where there is a pronounced sulfur attack, such as in smelting vessels used in the non-ferrous industry. This behavior arises from the formation of sulfates, which leads to densification by pore filling and the weakening of the brick bonds. C6 displayed the

highest corrosion resistance among the tested basic refractories. This specimen's improved chemical resistance can be related to the high concentration of forsterite in its structure; this phase has been reported to have higher corrosion resistance to sulfur gases than other common secondary phases found in MgO-based bricks, such as merwinite, monticellite, and larnite ⁽¹⁾. The forsterite in the brick was observed surrounding the MgO grains, which may have served as a barrier against corrosion.

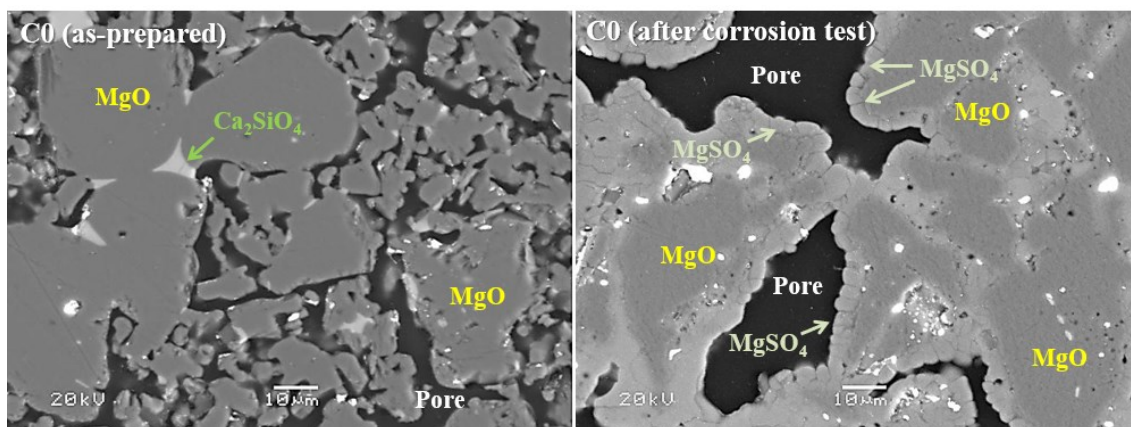


Figure 5.8: Backscattered electron SEM micrograph of C0 before (as-prepared) and after the corrosion test. The arrows indicate the presence of a thick MgSO₄ layer on the DBM grains.

5.4 CORROSION TEST II

Figure 5.2 shows a large variation in porosity as a function of the firing temperature for sample C5. Thus, an extra corrosion test was performed to evaluate the influence of the sample's apparent porosity by keeping the chemical composition constant. Three C5 samples fired at 1450 and 1630 °C and two C5 samples fired at 1550 °C were used in the corrosion test and the results are shown in Figure 5.9.

The variation in BD and AP and the sample's SO₃ content decreased with increasing the firing temperature (decreasing initial apparent porosity). Table V.4 exhibits the statistical analysis results obtained by repeated measures ANOVA for ΔBD and ΔAP. This test revealed that there is a statistically significant difference among the tested

samples for both ΔBD and ΔAP . As the obtained p-values are smaller than 0.05 for all comparisons, we can assume that the means are significantly different from each other. These results confirm that the initial apparent porosity of the samples influences their corrosion resistance to sulfur gases. The higher the initial apparent porosity, the lower the corrosion resistance due to the facilitated penetration of gases and the higher contact area between SO_3 and the basic refractory components.

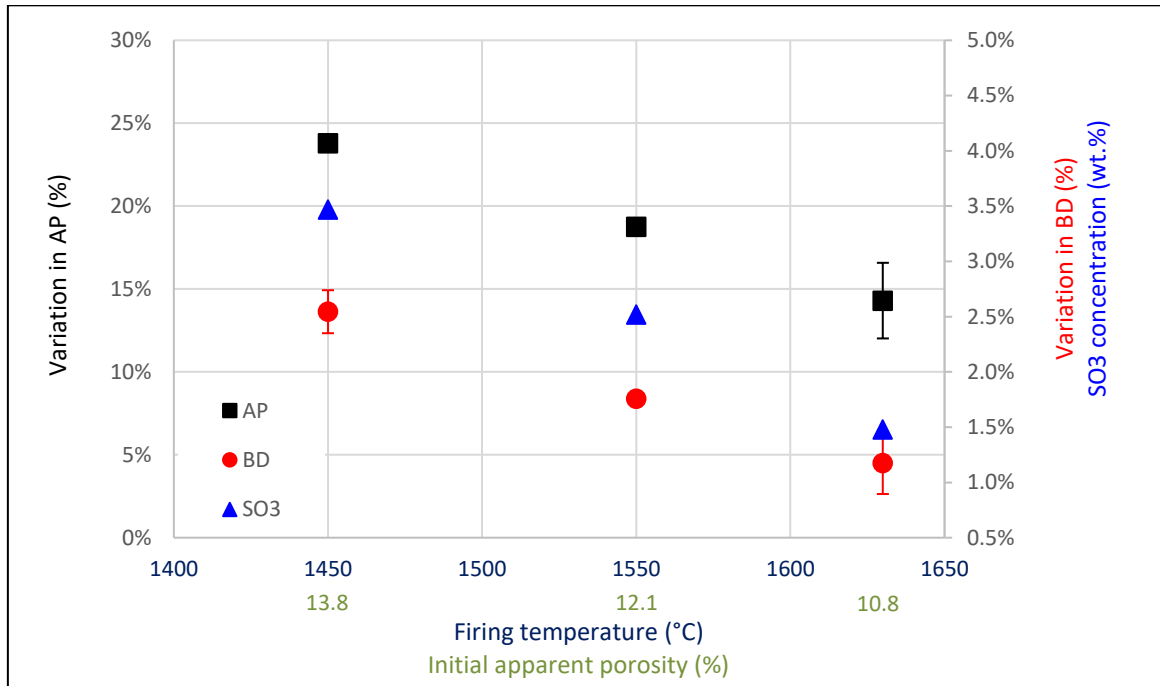


Figure 5.9: Variation in AP, BD, and SO_3 content as a function of the firing temperature and initial apparent porosity (Equations 4.1 and 4.2) for sample C5

Table V.4: F ratios and p-values obtained by repeated measures ANOVA for comparing samples C5 fired at 1450 °C, 1550 °C, and 1630 °C regarding the change in bulk density and change in apparent porosity.

| | ΔBD (g.cm ⁻³) | ΔAP (%) |
|---------|-----------------------------------|-----------------|
| F ratio | 16.868 | 44.164 |
| p-value | 0.0112 | 0.0019 |

5.5 CORROSION TEST III

Two samples corresponding to C0 and C6 (maximum and minimum C/S ratios, respectively) fired at 1450 and 1630 °C were used in corrosion test III to evaluate the combined effect of firing temperature/porosity and C/S ratio. The results of this third corrosion test are shown in Table V.5. As only two samples were used for each combination of recipe and firing temperature, no statistical analysis was performed.

Table V.5: Variation in AP, BD and SO₃ content as a function of the firing temperature and initial apparent porosity (Equations 4.1 and 4.2) for samples C0 and C6

| Sample (C/S) | C0 (2.9) | | C6 (0.3) | |
|-------------------------|-----------|-----------|-----------|-----------|
| | 1450 | 1630 | 1450 | 1630 |
| Firing temperature (°C) | 1450 | 1630 | 1450 | 1630 |
| initial AP % | 14.2 | 13.7 | 15.9 | 13.1 |
| Variation in BD (%) | 4.1 ± 0.2 | 3.4 ± 0.2 | 3.1 ± 0.0 | 1.8 ± 0.3 |
| Variation in AP (%) | 35 ± 1.9 | 31 ± 1.5 | 23 ± 0.1 | 15 ± 2.5 |
| SO ₃ (%) | 3.9 | 3.6 | 3.1 | 1.5 |
| Ca/Mg-Sulfate (%) | 2-5 | 2-5 | 2-5 | 0.5-2.0 |
| Forsterite (%) | - | - | 2-5 | 2-5 |

The results show that the sample C0 fired at 1450 °C had the lowest corrosion resistance among the tested samples, and only slightly higher Δ BD, Δ AP, and Δ SO₃ when compared to the same recipe fired at 1630 °C. Recipe C6 had overall higher corrosion resistance than C0, despite its higher porosity after firing at 1450 °C. This suggests that, in this specific test, the refractory's chemical composition (specifically its forsterite content) played a more important role than its physical properties when evaluating its corrosion resistance against sulfur gases. C6 fired at 1630 °C exhibited the highest corrosion resistance among the tested samples and a more significant improvement with increasing firing temperature when compared to C0-derived samples. This is related to the higher amount of liquid phase formed at 1630 °C for composition C6 compared to C0 (Figure 5.1), which promotes a more effective sintering process and eliminates pores. In addition, higher heat treatment

temperatures favor the formation and improve the properties of forsterite ⁽³⁰⁾, which, as previously mentioned, has high chemical resistance to the attack of sulfur gases.

6. CONCLUSIONS

The procedure used in this work to evaluate the corrosion resistance of MgO-based samples to sulfur gases is novel, simple, cost-effective, and reliable. The corrosion resistance of refractories can be investigated by measuring the changes observed in the samples' bulk density and apparent porosity after their exposure to sulfur gases. The smaller this difference, the higher the corrosion resistance of the examined material.

In corrosion test I, this procedure was used to investigate the effect of the C/S ratio on the corrosion resistance of basic refractories. The results obtained were validated by an in-depth statistical analysis conducted using ANOVA and post hoc Fisher LSD tests. The sample with the lowest C/S ratio (C6, C/S = 0.3) showed the best results in the test and, therefore, the highest corrosion resistance. The other tested compositions containing C/S values ranging from 0.5 to 2.3 showed similar results and lower corrosion resistance than C6. This behavior suggests that no linear correlation can be established between the C/S ratios from 0.3 to 2.3 and the refractory corrosion resistance against sulfur gases. Low values of C/S (< 0.5) promote the formation of forsterite as the primary interstitial phase, which, as opposed to MgO and other interstitial phases, does not react with sulfur gases to form magnesium and calcium sulfates. Significant amounts of forsterite in the brick (5-10%, as detected in C6) surround the MgO grains and act as a barrier, inhibiting their corrosion.

In corrosion test II, the influence of the refractory's initial apparent porosity (correlated to its firing temperature) on its corrosion resistance to sulfur gases was evaluated by keeping the chemical composition constant. The results were validated by a statistical analysis conducted using repeated-measures ANOVA. The difference in ΔBD and ΔAP among the samples was statistically significant. Thus, their initial apparent porosity is inversely correlated to their corrosion resistance to sulfur gases.

Corrosion test III compared the influence of the sample's C/S ratio with its apparent

porosity by simultaneously testing samples with maximum and minimum C/S ratio and firing temperatures. As expected, the sample with the highest C/S ratio and lowest firing temperature (C0 fired at 1450 °C) had the lowest corrosion resistance, while the sample with the lowest C/S ratio and highest firing temperature (C6 fired at 1630 °C) had the best results. When comparing sample C0 fired at 1630 °C to C6 fired at 1450 °C, the latter showed higher corrosion resistance, which suggests that the refractory's chemical composition (more specifically, its forsterite content) played a more important role than its physical properties. Due to the small sample size (n=2), these results could not be confirmed by statistical analysis.

The results obtained in this study confirm the applicability of this novel procedure to evaluate the corrosion resistance of basic refractories to sulfur gases. Statistically significant results were obtained to conclude that basic refractories that contain a substantial amount of forsterite (5-10%) can be considered more resistant to corrosion caused by sulfur gases than basic refractories having higher C/S ratios (≥ 0.5) and, therefore, negligible forsterite content. The sample's initial apparent porosity also plays a significant role in the refractory's corrosion resistance, once low initial AP can act as a physical barrier to decelerate the corrosion progression. This procedure can be applied to support the design of refractory linings for applications in which sulfur gases are present in the furnace atmosphere, such as in the non-ferrous industry.

7. SUGGESTIONS FOR FUTURE WORKS

- 1) Study of the C/S ratio range between 0.3 and 0.5 and its influence in the refractory's corrosion resistance.
- 2) Study of the amount of forsterite formed with a fixed C/S ratio (ex. C/S=0.3, varying CaO content) and its influence in the refractory's corrosion resistance.
- 3) Comparison between the corrosion resistance to sulfur gases of different types of sintered magnesia.
- 4) Performance of repetitive corrosion test cycles on the same set of samples to evaluate degradation of the refractory bonds. In this case, the samples would be fired at $> 1150^{\circ}\text{C}$ after each corrosion test to promote the decomposition of the sulfates formed. The destruction of bonds could be evaluated through CCS.
- 5) Evaluation of the corrosion resistance to sulfur gases of refractories commonly employed in the non-ferrous industry and the influence of their Cr_2O_3 content.
- 6) Evaluation of the corrosion resistance to sulfur gases of refractories commonly employed in the glass industry and the influence of their ZrO_2 content.

8. ACADEMIC PRODUCTION RELATED TO THIS WORK

- D.M. Fonseca, G.R. Pacheco, W. Moulin-Silva, G.E. Gonçalves, Novel test for evaluating refractory resistance against corrosion by sulfur oxides, Proceeding of the Biannual Conference of the Latin American Association of Refractories Manufacturers - ALAFAR, (2018), pp. 1–10, Medellin (Colombia).

- D.M. Fonseca, G.R. Pacheco, W. Moulin-Silva, G.E. Gonçalves, R. Neuböck, Development and applicability of a new corrosion test to quantify refractory wear due to gaseous sulphur oxides action, Proceeding of the Annual Conference of Metallurgists - COM, (2019), pp. 1–8, Vancouver (Canada).

- D.M. Fonseca, D. Gregurek, E.H.M. Nunes. Application of a novel and simple test to evaluate the corrosion resistance of magnesia-based refractories to sulfur gases, *Ceramics International* 46 (2020) 26160–26167, doi: 10.1016/j.ceramint.2020.07.113

9. REFERENCES

1. *Degradation mechanisms and use of refractory linings in copper production processes: A critical review.* Malfliet, A., et al. 2013, Journal of the European Ceramic Society, p. 005.
2. Gregurek, D. *RHI Magnesita Internal Customer Report 20040278.*
3. Reinharter, K. *RHI Magnesita Internal Research Report 20151245.*
4. *Novel test for evaluating refractory resistance against corrosion by sulfur oxides.* Daniela M. Fonseca, Graziella R. Pacheco, Wagner Moulin-Silva, Geraldo E. Gonçalves. Medellin, Colombia : ALAFAR, 2018. ALAFAR Conference.
5. *High temperature gaseous corrosion resistance of MgO-containing refractories – A comparative study.* Gerle, A., Podowórny, J., Wojsa, J. & Zelik, W. 2016, Ceramics International, pp. 15805-15810.
6. *Interaction of MgO-MgR₂O₄ (R: Al, Cr, Fe) refractories with SO₂-containing gases.* Fotoyi, N. & Eric, R. 2011, Southern African Pyrometallurgy, pp. 373-388.
7. Fotoyi, N. *Gas-refractory Interactions of Basic Refractories with Sulfur-bearing Gases Produced in Converter Furnaces during Extraction of Platinum Group Metals in Non-ferrous Industry. M.Sc. Dissertation.* Johannesburg, South Africa : University of the Witwatersrand, 2009.
8. *Investigations into kinetics and mechanism of gas-solid state processes in MgO-MgR₂O₄ (R:Al,Cr,Fe) spinels-SO₂-O₂ system.* Podwórny, J., Piotrowski, J. & Wojsa, J. 2008, Ceramics International, pp. 1587-1593.
9. *How To Deal With Alkali Infiltration In Mag-Spinel Bricks Used In Cement Rotary Kilns?* Pacheco, G. & Fonseca, D. St. Louis, USA : s.n., 2018. Refractory Ceramics Division Symposium on Refractories.

10. *Development and applicability of a new corrosion test to quantify refractory wear due to gaseous sulphur oxides action.* Daniela M. Fonseca, Graziella R. Pacheco, Wagner Moulin-Silva, Geraldo E. Gonçalves and Rainer Neuböck. Vancouver, CA : COM-Copper, 2019. COM-Copper 2019 Conference.
11. Weise, K. H. e Stern, E. L. *High Temperature Properties and Decomposition of Inorganic Salts.* Washington, DC : National Standard Reference Data Series - National Bureau of Standards, 1966.
12. Tagawa, Hiroaki. Thermal decomposition temperatures of metal sulfates. *Thermochimica Acta.* 80, 1984, pp. 23-33.
13. H., Kellog H. Critical review of sulfation equilibria. *Trans TMS-AIME.* 230, 1964, S. 1622-1644.
14. *Decomposition of metal sulfates - A SO₂-source for sulfuric acid production.* J. Hammerschmidt, M. Wrobel. s.l. : Sulphur and Sulphuric Acid Conference, 2009. Sulphur and Sulphuric Acid Conference 2009.
15. The Copper Industry: Occurrence, Recovery, and Consumption. www.knovel.com. [Online] 2001.
16. Aguiar, W. *Processo de fabricação de cobre: Paranapanema – Unidade Dias D´Avila.* Contagem : s.n., 2015.
17. Harbison-Walker Refractories Co. *Harbison-Walker Handbook of Refractory Practice.* Moon Township, PA : s.n., 2005.
18. *Microstructural analysis of magnesia bricks operating under oxidizing and reducing atmospheres in the regenerator condensation zone of glass melting furnaces.* Christian Majcenovic, Gerald Gelbmann, Rongxing Bei. s.l. : RHI Bulletin, 2014.
19. Zhaoyou, Chen. Refractories for RH Degassers and Ways of Improving Their Lining Life. *China's Refractories.*

20. Schacht, edited by Charles A. *Refractories Handbook*. s.l. : Taylos & Francis Group, 2004.
21. Christina Strelj, P. Wobrauschek, P. Kregsamer. X-ray Fluorescence Spectroscopy, Applications. *Encyclopedia of Spectroscopy and Spectrometry*. 1991.
22. Kohli, Rajiv. Methods for Monitoring and Measuring Cleanliness of Surfaces. [A. do livro] Rajiv Kohli and K.L. Mittal. *Developments in Surface Contamination and Cleaning*. 2012.
23. D. Gregurek, K. Reinharter, C. Majcenovic, C. Wenzl, A. Spanring. Overview of wear phenomena in lead processing furnaces. *Journal of the European Ceramic Society*. 35, 2015, pp. 1683-1698.
24. German, R. M. Introduction to liquid phase sintering. *Liquid Phase Sintering*. Boston, MA : Springer, 1985, pp. 1-11.
25. —. Sintering with a liquid phase. *Sintering: from Empirical Observations to Scientific Principles*. New York : Elsevier, 2014, pp. 247–303.
26. C.B. Carter, M. G. Norton. Sintering and grain growth. *Ceramic Materials - Science and Engineering*. New York : Springer, 2013, pp. 439-456.
27. M.A. Azmah Hanim, D. Brabazon, M.S.J. Hashmi. Cracks, microcracks, and fracture toughness of polymer composites: Formation, testing method, nondestructive detection, and modifications. [A. do livro] M. Thariq, N. Saba M. Jawaid. *Failure Analysis in Biocomposites, Fibre-Reinforced Composites and Hybrid Composites*. Cambridge : Woodhead Publishing, 2019, pp. 157-180.
28. Brown, A.M. A new software for carrying out one-way ANOVA post hoc tests. *Comput. Methods Programs Biomed.* 79, 2005.
29. G. Liu, Y. Li, T. Zhu, Y. Xu, J. Liu, S. Sang, Q. Li, Y. Li. Influence of the atmosphere on the mechanical properties and slag resistance of magnesia-chrome bricks. *Ceramics International*. 46, 2020, pp. 11225-11231.

30. *Characterization of forsterite ceramics*. K.Y. Sara Leea, K.M. Christopher Chin, S. Ramesh, J. Purbolaksono, M.A. Hassan, M. Hamdi and WD. Teng. 1, 2013, Journal of Ceramic Processing Research, Vol. 14, pp. 131-133.

APPENDIX

Table X.1: Bulk density, apparent porosity and cold crushing strength results of the original samples C0-C6 and RS after each firing temperature.

The results in bold correspond to the samples selected for corrosion test I

| | C0 | | | C1 | | | C2 | | | C3 | | | C4 | | | C5 | | | C6 | | | RS | | |
|-------------------------|-----------|------|-------------|-----------|------|-------------|-----------|-------------|------|-------------|------|------|-------------|------|------|-------------|------|------|-----------|------|-------------|-----------|------|-------------|
| C/S | 2.9 | | | 2.3 | | | 1.7 | | | 1.2 | | | 0.8 | | | 0.5 | | | 0.3 | | | - | | |
| Firing T (°C) | 1450 | 1550 | 1630 | 1450 | 1550 | 1630 | 1450 | 1550 | 1630 | 1450 | 1550 | 1630 | 1450 | 1550 | 1630 | 1450 | 1550 | 1630 | 1450 | 1550 | 1630 | 1450 | 1550 | 1630 |
| CCS (MPa) | 56 | 66 | 71 | 61 | 73 | 86 | 69 | 103 | 115 | 75 | 121 | 136 | 76 | 136 | 161 | 59 | 61 | 118 | 39 | 31 | 43 | 35 | 52 | 67 |
| BD (g/cm ³) | 3.04 | 3.04 | 3.05 | 3.04 | 3.04 | 3.05 | 3.03 | 3.05 | 3.07 | 3.04 | 3.07 | 3.08 | 3.03 | 3.09 | 3.12 | 3.01 | 3.06 | 3.11 | 2.91 | 2.97 | 3.03 | 3.07 | 3.10 | 3.12 |
| AP (%) | 13.9 | 13.9 | 13.7 | 14.1 | 14.0 | 13.7 | 14.1 | 13.8 | 13.4 | 13.7 | 13.1 | 12.7 | 13.6 | 12.0 | 11.1 | 14.1 | 12.7 | 11.0 | 16.2 | 14.6 | 13.1 | 18.6 | 18.2 | 17.1 |

Table X.2: Weight of the samples before and after the last two tests of corrosion test I

| | C0 | C1 | C2 | C3 | C4 | C5 | C6 | A | Box |
|---------------|---------------------|-----------|-----------|-----------|-----------|-----------|-----------|----------|------------|
| Test 3 | Before (g) | 88.7 | 86.9 | 83.2 | 84.7 | 82.4 | 86.1 | 88.4 | 9342.3 |
| | After (g) | 91.6 | 89.8 | 86.1 | 87.5 | 85.0 | 89.1 | 89.9 | 9143.8 |
| | Weight increase (%) | 3.3 | 3.4 | 3.5 | 3.3 | 3.1 | 3.4 | 1.7 | -2.1% |
| Test 4 | Before (g) | 87.5 | 87.1 | 84.2 | 82.0 | 85.2 | 83.9 | 86.7 | 9344.8 |
| | After (g) | 90.4 | 90.0 | 86.9 | 84.8 | 87.8 | 86.5 | 88.0 | 9145.2 |
| | Weight increase (%) | 3.3 | 3.3 | 3.3 | 3.4 | 3.0 | 3.1 | 1.5 | -2.1% |

Table X.3: Bulk density and apparent porosity of the original samples and the percentual change after each test (including SO₃ content) of corrosion test I

| | C0 | C1 | C2 | C3 | C4 | C5 | C6 | A | |
|---------------------------------|---------------------|------------|------------|------------|------------|------------|------------|-----------|------------|
| C/S wt | 2.9 | 2.3 | 1.7 | 1.2 | 0.8 | 0.5 | 0.3 | - | |
| Initial BD (g/cm ³) | 3.05 | 3.05 | 3.05 | 3.04 | 3.03 | 3.01 | 3.03 | 3.12 | |
| Initial AP (%) | 13.7 | 13.7 | 13.8 | 13.7 | 13.6 | 13.8 | 13.1 | 17.1 | |
| Test 1 | increase BD (%) | 4.1 | 3.9 | 5.1 | 3.8 | 3.7 | 3.1 | 1.7 | 0.4 |
| | decrease AP (%) | 45 | 43 | 50 | 44 | 44 | 40 | 20 | -1.8 |
| | SO ₃ (%) | 2.6 | 2.9 | 2.8 | 2.8 | 2.5 | 2.6 | 1.6 | 0.0 |
| Test 2 | increase BD (%) | 3.2 | 4.0 | 3.5 | 3.5 | 2.9 | 2.9 | 1.7 | 0.2 |
| | decrease AP (%) | 29 | 33 | 30 | 31 | 27 | 27 | 16 | -0.1 |
| | SO ₃ (%) | 3.6 | 3.3 | 3.5 | 3.5 | 3.2 | 3.6 | 1.8 | 0.0 |
| Test 3 | increase BD (%) | 3.6 | 4.1 | 3.3 | 3.4 | 3.2 | 2.9 | 2.0 | -0.3 |
| | decrease AP (%) | 30 | 33 | 27 | 29 | 28 | 26 | 17 | -3.3 |
| | SO ₃ (%) | 3.4 | 3.4 | 3.4 | 3.5 | 3.3 | 3.5 | 1.7 | 0.0 |
| Test 4 | increase BD (%) | 3.2 | 3.5 | 3.3 | 3.2 | 3.2 | 2.9 | 1.4 | -0.2 |
| | decrease AP (%) | 29 | 30 | 28 | 29 | 28 | 26 | 13 | -2.0 |
| | SO ₃ (%) | 3.6 | 3.4 | 3.4 | 3.6 | 3.1 | 3.4 | 1.5 | 0.0 |
| Average | increase BD (%) | 3.5 ± 0.4 | 3.9 ± 0.2 | 3.8 ± 0.9 | 3.5 ± 0.3 | 3.2 ± 0.4 | 2.9 ± 0.1 | 1.7 ± 0.2 | 0.02 ± 0.3 |
| | decrease AP (%) | 27 ± 16 | 28 ± 16 | 27 ± 18 | 27 ± 16 | 25 ± 16 | 24 ± 15 | 13 ± 8 | -1.4 ± 1 |
| | SO ₃ (%) | 3.3 ± 0.5 | 3.2 ± 0.2 | 3.3 ± 0.3 | 3.3 ± 0.3 | 3.0 ± 0.4 | 3.3 ± 0.5 | 1.7 ± 0.1 | 0.0 ± 0.0 |

Table X.4: Changes in bulk density and apparent porosity and SO₃/ MgSO₄ content of composition C5 after the corrosion test II

| Firing temperature (°C) | 1550 | 1630 |
|-----------------------------------|-------------|-------------|
| Initial AP (%) | 12.1 | 10.8 |
| Increase in BD (%) | 1.8 ± 0.0 | 1.2 ± 0.3 |
| Decrease in AP (%) | 18.8 ± 0.5 | 14.3 ± 2.3 |
| SO₃ content (%) | 2.5% | 1.5% |
| MgSO₄ (%) | 0,5-2% | 0,5-2% |